ZERNIKE PISTON STATISTICS IN TURBULENT MULTI-APERTURE OPTICAL SYSTEMS

THESIS

Joshua J. Garretson, Capt, USAF

AFIT-ENG-MS-20-M-023

DEPARTMENT OF THE AIR FORCE
AIR UNIVERSITY

AIR FORCE INSTITUTE OF TECHNOLOGY

Wright-Patterson Air Force Base, Ohio

AFIT-ENG-MS-20-M-023

ZERNIKE PISTON STATISTICS IN TURBULENT MULTI-APERTURE OPTICAL SYSTEMS

THESIS

Presented to the Faculty

Department of Electrical and Computer Engineering

Graduate School of Engineering and Management

Air Force Institute of Technology

Air University

Air Education and Training Command

in Partial Fulfillment of the Requirements for the

Degree of Master of Science in Electrical Engineering

Joshua J. Garretson, B.S.E.E.

Capt, USAF

March, 2020

AFIT-ENG-MS-20-M-023

ZERNIKE PISTON STATISTICS IN TURBULENT MULTI-APERTURE OPTICAL SYSTEMS

THESIS

Joshua J. Garretson, B.S.E.E.
Capt, USAF

Committee Membership:

Stephen Cain, Ph.D
Chair

Maj David Becker, Ph.D
Member

Capt Joseph Tompkins, M.S.E.E
Member

AFIT-ENG-MS-20-M-023

Abstract

There is an ever growing difficulty in acquiring an accurate and clear situational awareness of all objects in the orbit of Earth. The growing difficulty is a result of the shear number of objects being placed in orbit, advancing technology, and a growing threat from America's adversaries. There are currently several methods of detecting and tracking objects in orbit that include radar and optical telescopes. Optical telescopes have a better resolution and can yield better intelligence if they take advantage of the most up-to-date optical technology and astronomy practices. Some of these technologies include atmospheric monitors, adaptive optics, stellar interferometers, and fringe trackers. All of these technologies are an attempt to obtain a diffraction limited image buy canceling out the effects of the atmosphere.

There is currently a lack of research into how the atmosphere effects Zernike piston. This Zernike piston is a coefficient related to the average phase delay of a wave. Usually Zernike piston can be ignored over a single aperture because it is merely a delay added to the entire wavefront. For multi-aperture interferometers though piston cannot be ignored. The statistics of Zernike piston could supplement and improve atmospheric monitoring, adaptive optics, stellar interferometers, and fringe tracking. This research will focus on developing a statistical model for Zernike piston introduced by atmospheric turbulence.

Table of Contents

Page

Page

List of Figures

List of Tables

ZERNIKE PISTON STATISTICS IN TURBULENT MULTI-APERTURE OPTICAL SYSTEMS

I. Introduction

The defense of America's space assets are at a higher priority now than ever before. The space capabilities of America's rivals are worrying. The recent reestablishment of the U.S Space Command and the establishment of the sixth military branch of the U.S military, the United States Space Force, is testament to America's priority in countering this threat from our adversaries. The first point of order is to gain a better everyday understanding of the situation in orbit. Space Situational Awareness (SSA), is a must to defend our space assets not only from our adversaries but also from space debris. SSA can be accomplished in a variety of ways, whether it be with space based, ground based, radar, or optical telescopes.

1.1 The Problem

1.1.1 Problem Background

Since the time of Galileo the ground based optical telescope has been, and continues to be, the most valuable tool for observing objects in our orbit and solar system. In the previous decades though space based telescopes have shown promise, and many think they are the future of space imaging. Space based telescopes cost orders of magnitude more to not only build, but also to test and sustain than ground based. The Hubble Space Telescope needed to be sustained through the space shuttle program and can longer be sustained. The only advantage to being space based is

the ability to take higher resolution images. This is due to there being an absence of atmosphere. The atmosphere distorts the light as it passes through the medium. This distortion is the reason why the most advanced ground based telescopes in the world are located in only a couple locations like Hawaii or Chile. These locations have better seeing quality because the atmosphere distorts the light less. The ability to correct for this distortion is difficult, which led to the idea of space based telescopes. In recent years, some in the space imaging community have started arguing that ground based telescopes should get a second chance. Advances like adaptive optics, atmospheric sensors, and an understanding in atmospheric sciences have led to ground based telescope capabilities matching that of space based telescopes. This gives an obvious advantage to ground based telescopes because of the far cheaper life cycle cost. The Air Force Research Lab (AFRL), Directed Energy Directorate, is the current military office leading the research effort for imaging through the atmosphere. Further research into sensing and controlling atmospheric distortions is well worth the cheaper cost of ground based telescopes.

A type of telescope array called a stellar interferometer has shown the promise of having very fine resolution, sometimes orders of magnitude better than that of single aperture telescopes with adaptive optics. A subsystem of importance in interferometers is the optical delay line. The reason for this delay line is to simply match the optical path lengths in the two or more telescopes. If there is path difference the higher resolution suffers. Currently the U.S. Navy is the military leader of stellar interferometer research with their Navy Precision Optical Interferometer (NPOI).

A practice in astronomy that has shown promise is the combination of atmospheric monitoring, adaptive optics, long baseline stellar interferometry, and fringe tracking. These four separate technologies have been around for more than several decades but the practice of using all four together is relatively new. The first location to get close

was the Keck Observatory in Hawaii but this site had its challenges and funding ended for the Keck Interferometer program in 2012. The NPOI got some of their equipment but they lack complex, cutting edge adaptive optic systems. The most promising interferometer in the world is the Very Large Telescope Interferometer (VLTI) in Chile which is in operation and produces high resolution images comparable to the best NPOI images. The VLTI uses adaptive optics and has four massive 8.2 meter apertures and state of the art beam combination facilities. The only thing VLTI doesn't do is fringe tracking, which the NPOI does and is why the two have similar resolution currently. The VLTI is working on implementing fringe tracking and it's predicted that once it does the telescope will have a resolution of $0.0025 arcseconds$, a limiting magnitude of 14 at near-infrared, and cost of $19 million to build [1][2]. For comparison, the James Webb Space Telescope will have a resolution of $0.1 arcseconds$, a limiting magnitude of 34 at near-infrared, and a cost of $10 billion to build [3][4]. This means the VLTI will have a resolution 40 times greater at a mere thousandths of the cost, yet won't be able to see the very faint objects like distant galaxies. There is still work to be done to obtain the same amount of light collected as space based telescopes.

It is even theorized that an interferometer being built in New Mexico by New Mexico Tech could have resolutions 100 times greater than that of the James Webb Space Telescope. This interferometer is called the Magdalena Ridge Observatory Interferometer (MROI) and when completed will have baselines from $7.8m$ to $340m$ [5]. In fact one of its core missions is space situational awareness. It has received funds or aid from the Naval Research Lab (NRL), AFRL, the National Aeronautics and Space Administration (NASA), National Science Foundation, and the University of Cambridge. Figure 1 shows a conception of what the finished MROI will look like.

Further research into seeing through the atmospheric is advantageous in producing

Figure 1: An artists conception of the MROI being built currently in New Mexico.[5]

better, higher resolution images with ground based telescopes. This higher resolution is of great concern for SSA of objects in GPS and geosynchronous orbits (GEO). Geosynchronous orbit and global positioning system (GPS) orbits are at a far higher altitude than low earth orbit (LEO). LEO is an altitude of $2,000km$ or less, GPS constellations are usually above $25,000km$, and GEO, along with the graveyard orbit where GEO satellites are placed and deactivated, is near $35,800km$. Imaging and detecting objects at LEO is fairly easy while imaging and detecting objects of the same size in our GPS orbits, GEO, and farther are far harder. An analogy is how imaging Mars is far harder than imaging the moon even though Mars is bigger but much farther away.

Not only is this a military problem but also a public problem. A mission of NASA mandated by congress is to locate and warn the nation of possible asteroid collisions, also known as planetary defense. So far NASA has had trouble in completing this planetary defense mission for the same reasons. This is a capability gap in our space battle management and planetary defense systems that needs to be addressed before threats become reality.

1.1.2 Problem Statement

There is a need for further research into atmospheric sensing and optical stellar interferometry in order to lower costs of ground based optical SSA initiatives and raise the quality of intelligence gathered by these initiatives.

1.2 This Research

1.2.1 Basic Concepts

There is currently a lack of research into how the atmosphere effects something called Zernike piston. This Zernike piston is a coefficient related to the average phase delay of a wave. Usually Zernike piston can be ignored because it is a delay added to the entire wavefront. For interferometers though piston can not be ignored.

Current sensing methods of determining the main atmospheric parameters involve recording star jitter and using the statistics of the jitter to determine the parameters. Star jitter is caused mostly by air turbulence. The current methods use either outdated turbulence models or a faulty relationship between the star jitter and the parameters. Zernike tilt, which can be thought of as the average slope of a wavefront, along with a better turbulence model could be used to determine the atmospheric parameters.

1.2.2 Hypothesis

Lower order Zernike polynomial coefficient statistics of multi-aperture optical systems can be used for simulation of turbulence effects, especially fringe variance, and for measuring atmospheric turbulence parameters

1.2.3 Research Objectives

The following are the objectives that have been sought during the course of this research:

1. Develop a mathematical model between atmospheric turbulence and the Zernike piston and tilt coefficients.

2. Simulate the model and analyze the generated data.

3. Record interferometric fringe patterns and image jitters and compare this recorded data to the simulated data.

4. Explore possible uses for this model.

These objectives where chosen to support the problem statement and research hypothesis.

1.2.4 Approach

In order to prove the hypothesis and complete all research goals an approach was developed. First a turbulence model needs to be chosen. Then the mathematical model between this turbulence model and Zernike piston will be developed. Previous verified work done by several individuals will be used as a framework for this model. The same will then be done for Zernike tilt. Once both models are complete then simulations will be performed and data generated for analysis. An optical experiment will be performed to collect empirical data. This empirical data will be analyzed against simulated data to verify the accuracy of the method. After these basic steps are completed then several possible uses for this model will be explored until the research is due.

II. Background and Literature Review

As a wavefront passes through the atmosphere the nonuniform density of the atmosphere causes optical phase aberrations. The connection between these optical aberrations and air density is the index of refraction of air which is a function of density. The phase of the wavefront arriving at the pupil of an optical system will be referred to as a phase screen.

This phase screen can be equated to a sum of weighted, orthogonal polynomials called Zernike polynomials. Each weight coefficient would have a spatiotemporal variance and all will have some correlation with another. The covariance of the the Zernike coefficients for the atmospherically disturbed wave front are important in any optics field where images are being collected through atmosphere.

This chapter will begin with a description of Zernike decomposition and atmospheric turbulence models. It will then discuss previous efforts in statistical models and atmospheric sensing. The final sections of this chapter will explain interferometry to better understand why piston differential is important and how it can be used.

2.1 Zernike Decomposition

Optical aberrations can be modeled using Zernike phase decomposition which is the method of breaking up a phase screen into a sum of weighted polynomials defined on the unit circle. Zernike polynomials form an orthonormal basis which is especially useful. Noll [6] summarizes that "Typical interest in Zernike polynomials centers around a polynomial expansion of an arbitrary wave front over a circular aperture of arbitrary radius." For the purpose of this thesis, Cartesian coordinates will be used contrary to the polar coordinates. The lowest degree polynomial is unity. This polynomial is termed piston and can be described as the group delay of the wave front

or the delay as a whole the wave front has experienced. The next two polynomials are tip and tilt aberrations that ultimately shift images at a detector and are of the first degree. The polynomials keep increasing in degree until an appropriate number to estimate the shape of the phase screen under consideration is chosen.

Table 1 identifies nine polynomials, two different indexes used for those polynomials, and their common names. The universal nomenclature of Zernike polynomials takes the form Z_n^m, where n and m are non-negative integers with $n \geq m$. Zernike polynomials by definition have a radial range between $(-1, 1)$ which means that $\sqrt{u^2 + v^2} \leq 1$. Figure 2 shows what the first 21 Zernikes appear as in phase

Table 1: Zernike Polynomials

$\mathbf{Z_n^m}$	**OSA Index**	**Noll Index**	**Polynomial(Cartesian)**	**Name**
Z_0^0	0	1	1	Piston
Z_1^{-1}	1	3	$2v$	Tilt (Y-Tilt)
Z_1^1	2	2	$2u$	Tip (X-Tilt)
Z_2^{-2}	3	5	$2\sqrt{6}uv$	Oblique Astigmatism
Z_2^0	4	4	$\sqrt{3}(2(u^2 + v^2) - 1)$	Focus
Z_2^2	5	6	$\sqrt{6}(u^2 - v^2)$	Vertical Astigmatism
Z_3^{-3}	6	9	$2\sqrt{2}v(3u^2 - v^2)$	Vertical Trefoil
Z_3^{-1}	7	7	$2\sqrt{2}v[3(u^2 + v^2) - 2]$	Vertical Coma
Z_3^1	8	8	$2\sqrt{2}u[3(u^2 + v^2) - 2]$	Horizontal Coma

screen format. Piston, the top most phase screen in Figure 2, is flat and only contributes a constant phase shift over the phase screen. In single aperture telescopes, the majority of stellar telescopes, this constant phase shift doesn't contribute to atmospheric aberrations as observed at the detector. For this reason it is ignored in almost all single aperture applications. In most cases a good approximation of a atmospheric phase screen can be accomplished using the first 11 Zernikes. The reason for this is due to the nature of turbulence and the covariance of the Zernike coefficients which

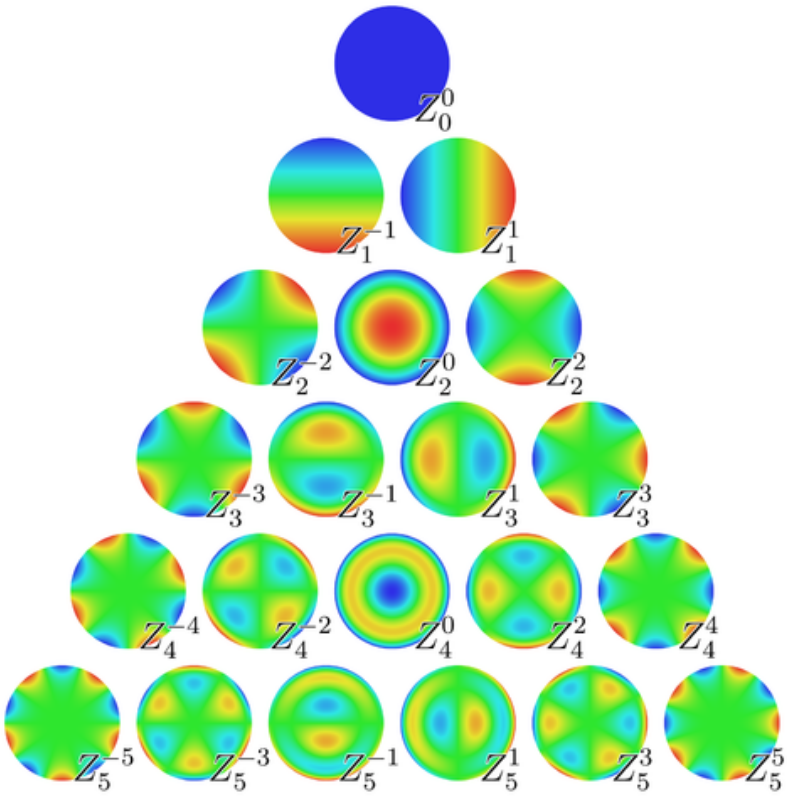

Figure 2: Phase screen representations of separate Zernike polynomials.

will be explained in the following subsections.

Because this paper draws from the work of Noll, the Zernike index used in [6] will be used, it has been termed the Noll sequential indices. This indices is defined by Eq. 1. In Noll's paper he described the patterns of the Fourier transforms of the Zernike Polynomials, $Q_j(f_u, f_v)$, over an aperture of radius R. He defined his index value j as:

$$j = (n^2 + n)/2 + |m| \tag{1}$$

Noll defined the the Fourier transform of the aperture weighted Zernike Polynomials as:

$$Q_j(f_u, f_v) = \mathcal{F}\left\{A(u,v)Z_j(u,v)\right\}_{(f_u,f_v)} \tag{2}$$

where $A(u,v)$ is the aperture function, $Z_j(u,v)$ is the chosen Zernike polynomial, and

f_u and f_v are spatial frequencies of u and v respectfully. This Q function takes the following pattern as defined by Noll:

$$if\ m = 0, \qquad \sqrt{n+1}\frac{J_{n+1}(2\pi\sqrt{f_u^2+f_v^2})}{\pi\sqrt{f_u^2+f_v^2}}(-1)^{(n)/2} \tag{3}$$

$$if\ m \neq 0, j\ is\ even, \quad \sqrt{2n+2}\frac{J_{n+1}(2\pi\sqrt{f_u^2+f_v^2})}{\pi\sqrt{f_u^2+f_v^2}}(-1)^{(n-m)/2} i^m \cos(m\tan^{-1}(f_u/f_v)) \tag{4}$$

$$if\ m \neq 0, j\ is\ odd, \quad \sqrt{2n+2}\frac{J_{n+1}(2\pi\sqrt{f_u^2+f_v^2})}{\pi\sqrt{f_u^2+f_v^2}}(-1)^{(n-m)/2} i^m \sin(m\tan^{-1}(f_u/f_v)) \tag{5}$$

Now that the Zernike decomposition has been explained in detail the second piece needed to explain to the covariance of Zernike coefficients will be discussed. Turbulence models are needed to explain how the turbulence effects the Zernikes both spatially and temporally.

2.2 Turbulence Models

Atmospheric turbulence models are used to aid in the correction of optical aberrations introduced by the atmosphere. These models are fluid dynamic models that use the index of refraction of turbulent eddies, which can be thought of as air packets. In the case of turbulent eddies being isotropic then the power spectral density (PSD) of the index of refraction is a function of one wave-number. Isotropic eddies will be assumed for this research.

The PSD of the index of refraction, $\Phi_\eta^K(f)$, was originally defined from the work of Kolmogorov [7] and can be seen as Eq. 6, which was drawn from [8]. The variable C_n^2 is the structure constant which serves as a measure of strength for the refractive

index fluctuations and f is generic spatial frequency in any 2-D spatial direction.

$$\Phi_{\eta}^{K}(f) = 0.033 C_n^2 (f)^{-11/3} \tag{6}$$

During the course of this thesis, the PSD of the phase fluctuations will be used instead of the PSD of the index of refraction. The phase fluctuation is directly related to the index of refraction fluctuation. The PSD of the phase fluctuations, $\Phi_{\Theta}^{K}(f)$, can be seen below as [6][9][10]:

$$\Phi_{\Theta}^{K}(f) = 0.0022896 r_0^{-5/3} (f)^{-11/3} \tag{7}$$

where r_0 is the seeing parameter, which is a function of the refraction index structure constant, C_n^2, and average wavelength, λ_0. The seeing parameter was first introduced by Fried [8] and is a parameter of the atmosphere. While Kolmogorov turbulence predicts the PSD of the inter-range frequencies accurately, it fails at lower and higher spatial frequencies [8]. For those lower and higher frequencies other turbulence models must be used.

2.2.1 Von Karman Turbulence

A modified version of Kolmogorov turbulence that is widely used is von Karman turbulence [11] [12] [9] [13]. This model adds a constant value bias to the spatial frequency. As seen in Eq. 8 the constant value is f_0 which is the inverse of a parameter called the outer scale or L_0.

$$\Phi_{\Theta}^{V}(f) = 0.0022896 r_0^{-5/3} (f^2 + f_0^2)^{-11/6} \tag{8}$$

This additional value drives the power to a constant at lower frequencies instead of it going to infinity as frequencies approach zero, which can be observed in Figure 3 In essence it acts as a low pass filter and removes the non-integrable pole at $f = 0$. This model is more realistic than Kolmogorov's due to there being a finite amount of air in the atmosphere [8].

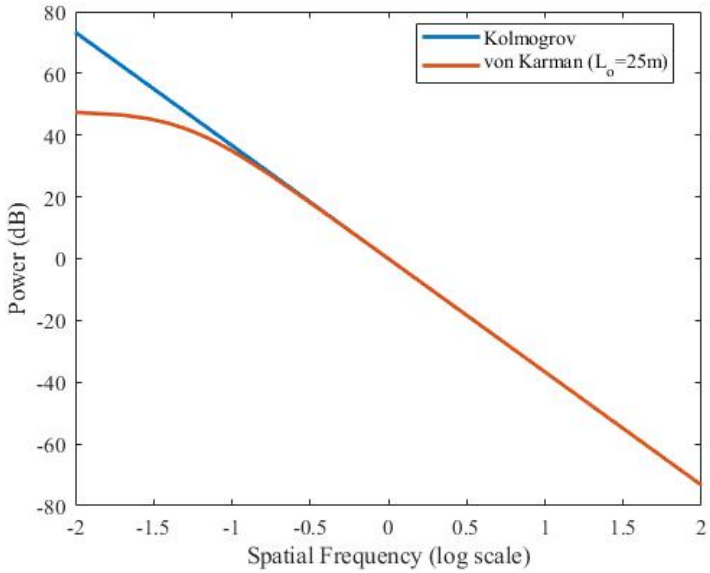

Figure 3: Comparison between the PSD of Kolmogorov and von Karman turbulence

2.2.2 Other Outer Scale Models

Since the shape of the spectrum is unknown, various other models have been theorized that include the outer scale parameter. Among them are the Exponential and Greenwood [12][14]. Exponential and Greenwood turbulence can bee seen by Eq. 9 and Eq. 10 respectfully. These models still hold close to the Kolmogorov model in the inter-range of the spectrum but break from Kolmogorov in lower frequencies. As seen in Figure 4 these models still approach infinity as frequencies approach zero but

they approach infinity slower than the Kolmogorov model does.

$$\Phi_{\Theta}^{E}(f) = f^{-11/3}(1 - e^{-f^2/f_0^2}) \tag{9}$$

$$\Phi_{\Theta}^{G}(f) = (f^2 + f_0 f)^{-11/6} \tag{10}$$

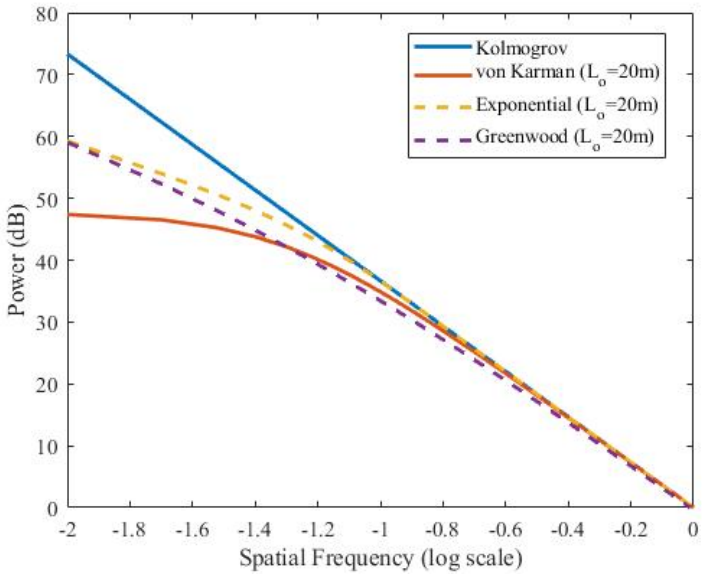

Figure 4: Comparison between Kolmogorov, von Karman, exponential, and Greenwood index of refraction PSD models.

Turbulence models along with Zernike decomposition is all that is needed to create a statistical model of how the atmosphere effects a wavefront. This statistical model will now be explained.

2.3 Covariances of Zernike Coefficients

The covariance of the coefficients of Zernike polynomials is a useful data point for several electro-optics subjects. If known it can be used to simulate phase screens, as control input to adaptive optics systems, and to find atmospheric parameters if

unknown. Phase is not defined on the unit circle but is defined within an arbitrary radius R. In the case of this thesis, and in the case of Noll's work [6], a circular aperture, $A(u,v)$, defined in Eq. 11 will be used for all apertures:

$$A(u,v) = \begin{cases} 1 & , \quad \sqrt{u^2+v^2} \leq 1 \\ 0 & , \quad \sqrt{u^2+v^2} > 1 \end{cases} \tag{11}$$

A phase screen, $\Theta(x,y)$, is the sum of all weighted polynomials as seen in Eq.12:

$$\Theta(x,y) = \Theta(Ru,Rv) = \sum_j a_j Z_j(u,v) \tag{12}$$

where the phase screen is defined over x and y and the Zernike polynomial is defined over the unit circle coordinates u and v. Again, Z_j is the jth Zernike polynomial and a_j is the jth Zernike coefficient. With this in mind, the definition of any Zernike coefficient can be defined as Eq.13.

$$a_j = \int\int A(u,v) Z_j(u,v) \Theta(Ru,Rv) du dv \tag{13}$$

It is assumed that Zernike coefficients of atmospheric phase screens are zero mean, Gaussian random variables. A covariance of two coefficients can hence be written as:

$$\left\langle a_j^* a_{j'} \right\rangle = \left\langle \int\int A^*(u,v) Z_j^*(u,v) A(u',v') Z_j'(u',v') \Theta^*(Ru,Rv) \Theta(Ru',Rv') du dv du' dv' \right\rangle \tag{14}$$

due to the aperture function and Zernike polynomial not being random processes the expected value can be closed onto the phases in Eq. 14 leading to:

$$\left\langle a_j^* a_{j'} \right\rangle = \int\int A^*(u,v) Z_j^*(u,v) A(u',v') Z_{j'}(u',v') \left\langle \Theta^*(Ru,Rv) \Theta(Ru',Rv') \right\rangle du dv du' dv' \tag{15}$$

The expected value of the product of the phase with its complex conjugate is the definition of autocorrelation of the phase hence:

$$\left\langle a_j^* a_{j'} \right\rangle = \int\int A^*(u,v) Z_j^*(u,v) A(u',v') Z_{j'}(u',v') \Gamma_\theta(Ru - Ru', Rv - Rv') du dv du' dv' \tag{16}$$

where Γ_θ is the autocorrelation function of the fluctuating phase. Noll then transforms Eq. 16 to the spatial frequency spectrum as seen below. This transformation involves the Wiener-Khinchin theorem and scaling property of Fourier transforms, and a proof can be found in appendix A.

$$\left\langle a_j^* a_{j'} \right\rangle = R^{-2} \int\int Q_j^*(f_u, f_v) Q_{j'}(f_u, f_v) \Phi_\theta(f_u/R, f_v/R) df_u df_v \tag{17}$$

The reason for writing in the frequency spectrum is to allow the use of the phase PSD as discussed in section 2.2. Noll's results for the normalized covariance of Zernike coefficients 2 through 9 can be seen in table 2. It should be noted that piston, tilt, and tip aberrations have the greatest variances of any other aberration introduced by the atmosphere.

Table 2: Normalized Zernike coefficient covariance matrix as calculated by Noll

j - index	2	3	4	5	6	7	8	9
2	0.448	0	0	0	0	0	0.0142	0
3	0	0.448	0	0	0	0.0142	0	0
4	0	0	0.0232	0	0	0	0	0
5	0	0	0	0.0232	0	0	0	0
6	0	0	0	0	0.0232	0	0	0
7	0	0.0142	0	0	0	0.00619	0	0
8	0.0142	0	0	0	0	0	0.00619	0
9	0	0	0	0	0	0	0	0.00619

There have been previous attempts to compute Zernike coefficient covariance using von Karman turbulence instead of Kolmogorov turbulence [15][16][17]. All of these

efforts used Noll's work as a basis and interchanged the Kolmogorov PSD for the von Karman PSD. They however approximate the integral formed by this substitution in order to solve it which yield different results to this thesis which analyzes the integral using a computer. These models also, as of yet, are not verified with empirical evidence.

2.4 Current Atmospheric Profiling and Monitoring Techniques

There are a mass of different devices and techniques currently used to monitor or profile the atmosphere. Atmospheric profiling is developing an understanding of the properties of individual layers of atmosphere at different altitudes from observing the entire path. Monitoring is having an apprehension of just the sum of the layers or the entire atmosphere along a certain path. Profiling is useful when observing entirely through the atmosphere and partially through the atmosphere but it is difficult to do. Some profiling methods only profile the atmosphere partially, up to or above a certain altitude. Monitoring is useful when observing entirely though the atmosphere and is relatively easy because only a couple data points are needed. For the sake of this paper there will be a focus on monitors and profilers that can make observations through the entire atmosphere.

Lombardi, et al.[18], addresses a monitor called the Differential Image Motion Monitor (DIMM). This type of monitor looks at the light of a star using two or more optical paths, usually with an aperture masked telescope. The two paths create two separate images of the same star. Figure 5 is a visual description of the device. The covariance and variance of the image motion gives enough information to estimate the seeing parameter r_0. This technique assumes Kolmogorov turbulence so outer scale is assumed to be infinite. It is important to note that DIMM relates the image motion of the star to the spatial rate of change, or the derivative of the wave front with

respect to x and y, also known as angle of arrival [19]. Angle of arrival is different than Zernike tilt. While it is true that Zernike tilt is the average slope of the wave front, the average slope isn't always the derivative, hence the two are not the same and can yield different results. Tokovinin [20] argues that DIMM actually measures Zernike tilt variances and not that of angle of arrive variance and also argues that DIMM be modified to follow von Karman turbulence.

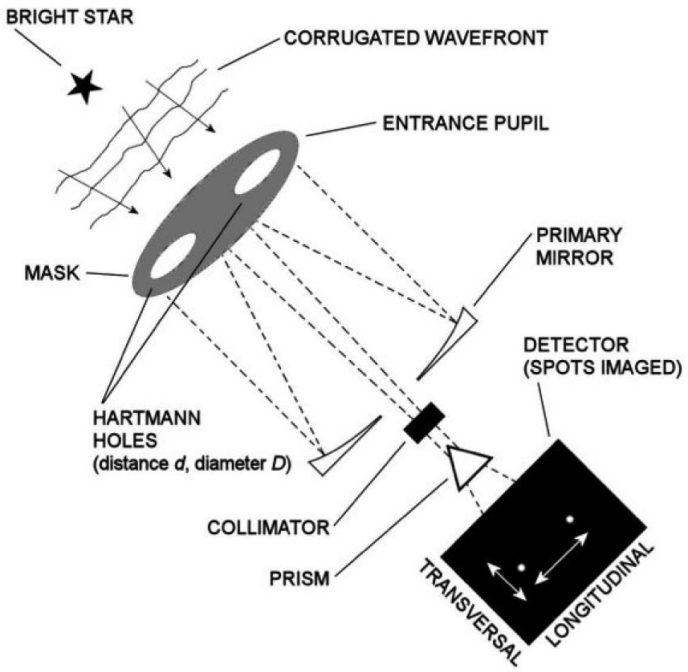

Figure 5: Visual layout of a DIMM [18]

A profiler of interest is the Scintillation Detection and Ranging (SCIDAR) technique. SCIDAR according to Lombardi [18], "extrapolates the OTP [turbulence profile] of the whole atmosphere up to 20-25 km above surface, with a resolution of few hundreds meters by measuring the spatial correlation of the scintillation produced on a telescope pupil plane by a double star target." Scintillation is change in intensity of light due to atmospheric turbulence. The limiting factor in this method is the need for a 'double star target' which is uncommon. The aperture of this device also must be larger than 1 meter to operate effectively leading to it being costly.

The last method to discuss is the Generalized Seeing Monitor (GSM) [14]. This monitor was developed using the von Karman turbulence model and uses image motion like DIMM. Also like DIMM, the GSM uses angle of arrival variance and covariance instead of the Zernike tilt variance and covariance. In a sense, GSM is a von Karman version of DIMM although there are several other differences between the two. The GSM measures the seeing parameter, r_0, and also the outer scale, L_0, but can also determine other parameters not of interest in the paper like isoplanatic angle and coherence time. It can do this by using four apertures instead of just two.

In summary, monitors and profilers in use have not taken full advantage of both Zernike decomposition and non-Kolmogorov turbulence to achieve atmospheric seeing. Another missed opportunity for seeing monitors has been interferometry which will be described in the next section.

2.5 Atmospherically Induced Piston Differential

The main concern of interest in of this thesis is modeling the statistics of path difference and piston differential using Zernike decomposition as stated in Chapter 1. Zernike decomposition, Zernike covariance, and interferometry have been explained to gain some understanding of how to achieve this goal. This section will describe what piston differential is and how it is related to path difference.

Phase differential is the difference in two wave fronts. Piston differential is the difference of two wave front averages or the difference in the Zernike piston coefficients. This research is concerned with the difference in two Zernike pistons. Figure 6 illustrates piston differential of a wave front above the aperture plane for an interferometer.

The total wave front over the entire area of the apertures and baseline is distorted by the atmosphere. The wave front arrives at one aperture before another causing a

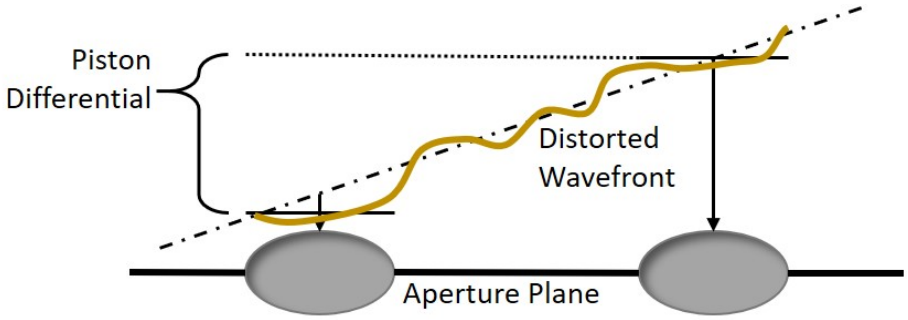

Figure 6: The effects of atmospheric distortion on path difference

temporal delay. This temporal delay can be translated into a path delay because the speed of light is known. Hence, while the piston of one aperture is meaningless the piston difference between two apertures is a cause of great concern when trying to generate a fringe pattern.

2.6 Interferometry

In order to better understand how an interferometer works, this section will begin by discussing how an optical system can take advantage of the wave nature of light to produce intensity patterns with more spatial frequency information than a normal diffraction pattern. Coherence, or correlation of a field, will be discussed to an appropriate level to gain an understanding of why certain patterns form in the intensity seen at an interferometer's detector. After a discussion on the effect of coherence, and how temporally delaying light effects the intensity, the natural causes of delay will be explained. The natural cause of concern with respect to this research is atmospheric delay or delay caused by the atmosphere.

2.6.1 Coherence

In wave optics the spatial and temporal correlation of light fields can be described by correlation functions, also known as coherence functions in optics. Even though

it's not a complete description, this coherence function gives a satisfactory statistical description of the light for modeling an optical system. Fields can be both spatially coherent and temporally coherent.

2.6.1.1 Definitions

A way to observe the coherence of light is with an interferometer. An interferometer uses the spatial and temporal coherence of light to create interference patterns. If the light is more coherent the number fringes will be greater, and vice versa incoherent light forms little to no fringe patterns.

Terms to consider while experimenting with coherence and interferometers are:

- *Fringe (Interference) Pattern*- The pattern made by the interfering fields.
- *Complex Degree of Coherence*- a functional degree of spatial and temporal coherence.
- *Coherence Envelope*- The area where the detect-ability of a fringe pattern is most likely. Usually the area within the first null of the fringe pattern.
- *Optical Path Difference or OPD*- A difference in the total distance light must travel from source to sensor in the two or more optical paths of an interferometer. Also referred to as path error in the context of matching path lengths.

For the purpose of simplicity, the following equations describing interferometry are only in the y-direction.

2.6.1.2 Spatial Coherence

Spatial coherence is concerned with the ability of light to interfere with a spatially shifted version of itself. The famous Young's experiment demonstrates the ability of light to interfere with itself spatially and proved the wave nature of light. The

experiment calls for light from a coherent, lower bandwidth source to be propagated through two pinholes. The light from the pinholes then propagates to a detector plane but the waves from the two pinholes interfere during the propagation. A set up of Young's experiment can be seen by Figure 7. The arrows right of the detector plane mark where intensity peaks.

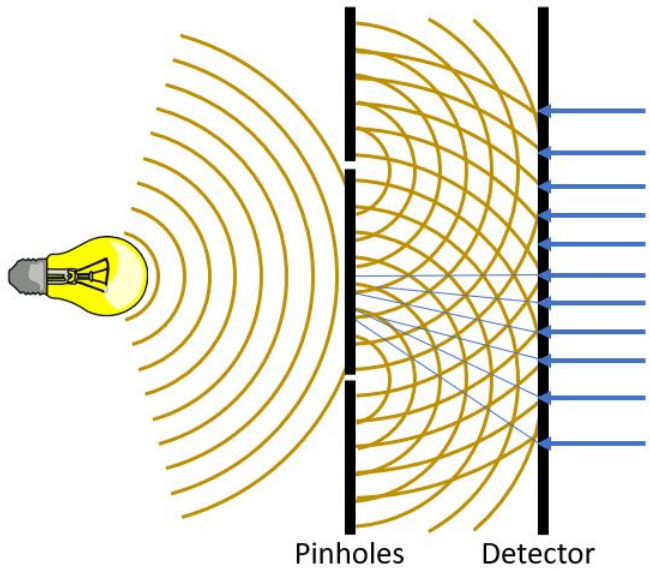

Figure 7: Young's Experiment

The intensity at the detector of Young's experiment, $I_D(y)$, is described by Goodman [8] as:

$$I_D(y) = 2I_0 \left[1 + \mu(P_1, P_2) cos\left(\frac{2\pi B}{\lambda_0 z} y\right)\right] \tag{18}$$

where P_1 and P_2 are the points where the pinholes are located, $\mu(P_1, P_2)$ is the complex coherence factor or a degree of spatial coherence between pinhole 1 and 2. I_0 is a constant intensity produced from one pinhole. Notice that the frequency of the cosine function is dependent on the baseline B, or spacing of the pinholes. The variable λ_0 is the average wavelength. In this case the pinholes are assumed to be ideal and z is the distance in between the pinhole plane and detector plane.

There are many methods of generating spatially incoherent light but the best

example of spatially incoherent light is natural light from our sun. The Van Cittert–Zernike theorem [8] implies that as spatially incoherent light propagates away from its source it becomes more coherent. Light from a star that is light-years away is coherent while light very close to a star, such as our own sun, is incoherent due to the way it is produced and the size of the sun. The area of the object generating or reflecting the light is another factor that contributes to spatial coherence. Smaller surface areas produce or reflect light that is more spatially coherent than larger surface areas. The area where light is spatially coherent is the coherence area and can be estimated by the ratio:

$$A_C \approx \frac{(\lambda_0 z)^2}{A_O} \tag{19}$$

where A_O is the area of the object producing or reflecting the light and z is the distance to the object. These attributes are important in characterizing the coherence of light being reflected off of satellites and other near earth objects. The smaller an object, the more difficult it is to see with a classical telescope. This is due in part by there being less reflected light, but these smaller objects produce light with higher spatial coherence.

2.6.1.3 Temporal Coherence

Light may interfere with a time-delayed wave when the delayed wave is identical or by some degree spatially coherent. Temporal coherence is concerned with this ability of light to interfere with a time-delayed version of itself. If the waveform remains constant throughout time, then it will be perfectly temporally coherent throughout time. The Michelson interferometer demonstrates the temporal coherence by splitting a beam, delaying one path by a distance, and then recombining the beams before detection. While the original purpose of the Michelson interferometer was to test the discredited theory of luminous aether it has many applications today. Figure 8 shows

the set up of the Michelson interferometer.

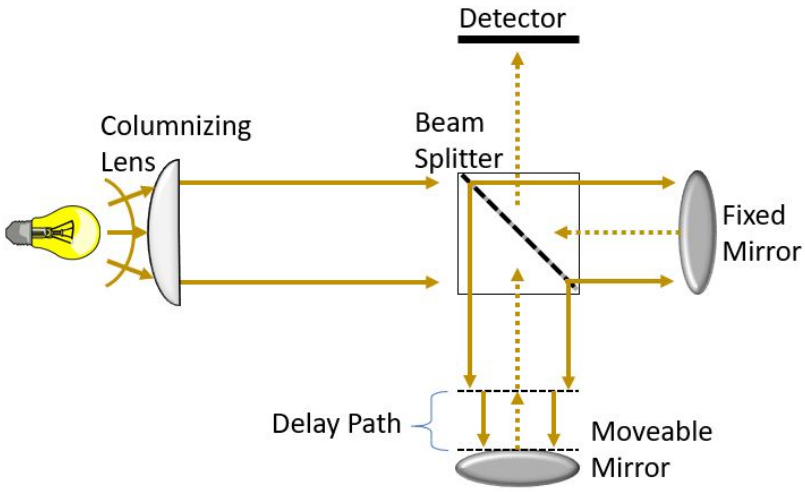

Figure 8: The Michelson Interferometer

The intensity at the detector of this temporal interferometer is given by Goodman [8] as:

$$I_D(d) = 2I_0 \left[1 + \gamma\left(\frac{2d}{\lambda_0}\right) cos\left(\frac{4\pi d}{\lambda_0}\right)\right] \tag{20}$$

where γ is the complex degree of self-coherence and is a function of time delay. Notice that the cosine in this intensity is a function of delay which in this case is $2d$ or twice the distance of the delay due to the light traversing the delay path twice.

2.6.2 Temporal Delay in Spatial Interferometers

In the example of Young's experiment temporal coherence was ignored, yet spatial interferometers do have temporal coherence effects. These effects will now be accounted for in order to better understand why path difference is important. Goodman [8] explains in short that the spatial coherence is responsible for the coherence envelope at zero path length difference, while temporal coherence is responsible for the tapering out of the fringes as path length difference grows. Figure 9 shows a stellar interferometer and an example of how path length difference is introduced. In this

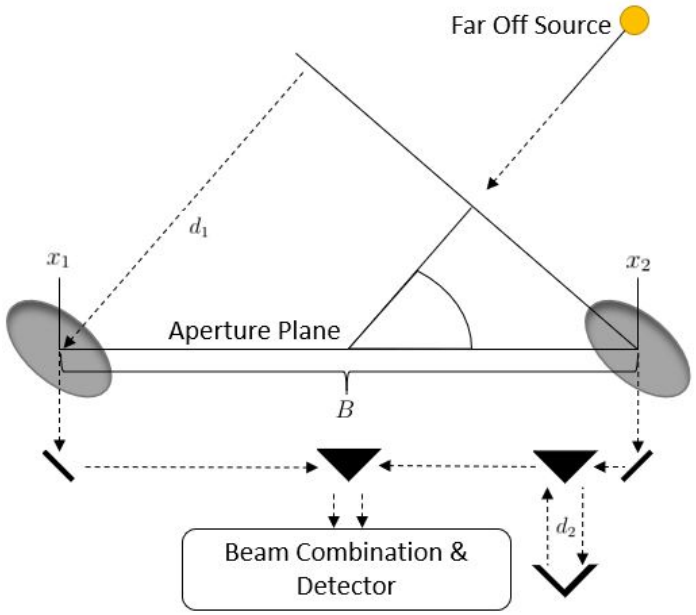

Figure 9: Typical Stellar Interferometer

figure, d_1 is a optical path difference introduced simply by positioning the apertures to observe a source of axis. The value d_2 is the OPD built into the interferometer to compensate for this path difference. Trigonometric causes are the main source of path difference but are easily remedied by setting d_2 equal to d_1.

The temporal coherence introduced by the path difference makes this spatial interferometer into a spatiotemporal interferometer. The intensity seen at the detector when the apertures are pinholes can then be given as:

$$I_D(y;\tau) = 2I_0\left[1+\gamma(P_1,P_2;\tau)cos\left(\frac{2\pi}{\lambda_0}\left(\frac{By}{z}-\Delta d\right)\right)\right] \tag{21}$$

Notice that the path difference Δd causes a phase shift in the fringe patterns. It will also effect the complex degree of coherence $\gamma(P_1,P_2;\tau)$, which is a degree of how spatially and temporally correlated the two interfering waves are. If we were to use identical apertures instead of pinholes an additional diffraction pattern would be seen.

Equation 22 is a description of the intensity with apertures.

$$I_D(y;\tau) = 2I_0D^4 sinc^2\left(\frac{Dy}{\lambda_0 z}\right)\left[1+\gamma(P_1,P_2;\tau)cos\left(\frac{2\pi}{\lambda_0}\left(\frac{By}{z}-\Delta d\right)\right)\right] \tag{22}$$

The addition of temporal coherence in spatial interferometers will directly have an effect on the fringe patterns by changing their phase and amplitude. The larger the path difference the greater the phase shift and effect on fringe depth, also known as visibility.

2.6.3 Visibility and Fringe Tracking

Analyzing the fringes is important in order to back track a fringe pattern to solve for any path difference. The act of analyzing a fringe and estimating the path difference from this analysis is called fringe tracking. Fringe tracking is used to lower the interferometric path difference as much as possible.

2.6.3.1 Visibility

Classical fringe analysis started with the Michelson fringe visibility which was defined by Michelson [21] as the following:

$$\mathcal{V} \triangleq \frac{I_{max}-I_{min}}{I_{max}+I_{min}} \tag{23}$$

where I_{max} is the max intensity of the fringe pattern and I_{min} is the minimum intensity. Visibility measures the normalized depth, or amplitude, of the fringes. This means that visibility is directly proportional to the complex degree of coherence:

$$\mathcal{V} \propto |\boldsymbol{\gamma}(P_1,P_2;\tau)| \tag{24}$$

This classical method of measuring visibility is not entirely useful for determining path difference though. When there are very weak fringe patterns, or none at all, the pattern introduced by the diffraction of the apertures maybe measured as a fringe. This produces higher visibility measurements than there actually should be.

Fourier analysis of fringe patterns is advantageous because it allows for analysis of the frequency of fringes. After taking the Fourier transform of the interferogram, $i_D(f) = \mathcal{F}\{I_D(y)\}$, a new visibility measurement is needed. This measurement will be the ratio of peaks in the Fourier transform which is defined by Equation 25. One peak is from the lower frequency of the diffraction pattern. The other peak is from the higher frequency of the fringe pattern. As fringes decrease with path difference, the ratio will decrease as well. The more prevalent the fringes are then the higher the second peak and ratio. This ratio will be termed the Fourier visibility.

$$F\mathcal{V} \triangleq \frac{i_{2^{nd}Peak} - i_{min}}{i_{max} + i_{min}} \tag{25}$$

where $i_{2^{nd}Peak}$ is the value of the second highest peak which is related to the frequency of the diffraction pattern. The variables i_{max} and i_{min} are the maximum and minimum values of i_D. The simulated Fourier visibility of a rectangular spectrum was plotted against the OPD for Figure 10. As the difference grows fringes decrease. The lowest point of this visibility occurs close to $8\mu m$ which was the coherence length of the rectangular spectrum being simulated. Different shaped spectrums will produce different visibilities per the OPD. The direct relationship of a fringe pattern to total OPD is an important step to estimating path difference.

2.6.3.2 Current Fringe Tracking Methods

The are currently three widely used fringe trackers in use today. These are discussed in detail in the course notes of "Principles of Long Baseline Stellar Interfer-

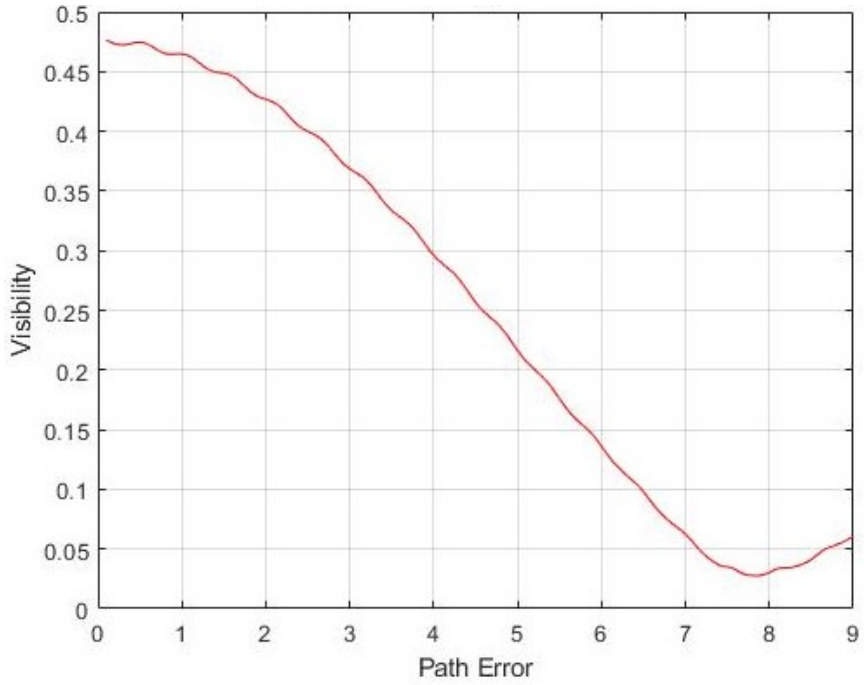

Figure 10: Fourier visibility, $F\mathcal{V}$, per path error (μm) for a rectangular spectrum of $500nm$ to $560nm$

ometry" [22]. These three methods are coherence envelope, group delay, and phase tracking. Coherence envelope tracking does a sweep of the delay several times greater than the coherence length. The delay is then set to the location of the greatest number of fringes. Group delay tracking uses the Fourier visibility described previously to determine path error and sets the delay accordingly. Phase tracking involves measuring the phase of the fringe pattern and relating the phase back to a path difference. This is done by modulating the path delay by a known amount at least three times in order to collect three different fringe patterns. By analyzing these three different images the three unknowns in Eq. 22 of source intensity, complex degree of coherence, and fringe phase can be solved for. As seen in Eq. 22, the phase of the fringe is directly related to the path error. The delay is then adjusted based of this path error.

Out of all of these fringe tracking methods, group delay is the most simple and

least time consuming method to implement. All visibility mapping of a source can be done upfront or if the spectrum of the source is known then visibility per path difference can be simulated. Only one image is needed to obtain a path difference. Coherence envelope tracking is only as accurate as the baseline sweep, and must be done again when fringes are reduced due to the changes of the atmosphere over time [22]. Phase tracking also modulates the delay path, records, and analyzes three or more images compared to group delays one image.

2.7 Summary of Background and Literature Review

The background of this research covered an array of optical studies. All of these areas of study, along with several others, were needed to achieve the research goals laid out in chapter 1. The main area of concern though is that of Zernike coefficient covariance. The background of Zernike covariance and von Karman Turbulence are the basis of defining piston covariance.

III. Methodology

In order to obtain piston variance and the autocovariance the von Karman turbulence model is chosen instead of the Kolmogorov turbulence model since piston variance in the Kolmogorov model is assumed to be infinite. This is due to the fact that the Kolmogorov phase PSD approaches infinity as spatial frequency approaches zero. In reality this assumption is untrue and finite piston variance can be seen in interferometry. The path error in interferometers is in fact the difference in mean phase error between two apertures. The piston Zernike can be defined as the mean phase error. Since the phase error has a finite variance then the piston Zernikes must have a finite variance as well. For this reason, von Karman turbulence is chosen because it has a finite PSD as spatial frequencies approach zero.

The two atmospheric variables needed to obtain piston variance are the seeing parameter and outer scale. This is because the piston variance is going to be a function of the von Karman PSD. This leads to the piston variance and autocovariance ultimately being a function of these two variables. In order to experimentally verify the model, a method of measuring the seeing parameter and outer scale needed to be chosen. Using the piston variance model to be discussed as a baseline, a similar model was created for tilt. There will be an explanation of the calculated tilt variance and covariance and how it is used in data collection later in this chapter. The optical setup for data collection will be described near the end of the chapter as well.

3.1 Variance of Piston

3.1.1 Derivation

The variance of piston is simply the variance of the mean phase over a certain area. As the turbulent air changes its mean density throughout the path of the light, then

the mean phase of the wave will change as well. When the light arrives at the aperture the mean phase will be the piston. As stated previously, the Zernike polynomial for piston is simply unity. Taking the definition of Zernike coefficient covariance given by Noll, Eq. 17, and using PSD of von Karman turbulence Eq. 8, the following equation is formed:

$$\langle a_1^* a_1 \rangle = R^{-2} \int\int |Q_1(f_u, f_v)|^2 \frac{0.022896 R^{11/6}}{r_0^{5/3}} (f_u^2 + f_v^2 + R^2 f_0^2)^{-11/6} \, df_u df_v \quad (26)$$

where again, r_0 is the seeing parameter, f_0 is the inverse of the outer scale, R is the radius of the apertures, and f_u and f_v are spatial frequencies. By moving all constants and variables independent of spatial frequencies out of the integrals we are left with:

$$\langle a_1^* a_1 \rangle = 0.022896 \left(\frac{R}{r_0}\right)^{-5/3} \int\int |Q_1(f_u, f_v)|^2 (f_u^2 + f_v^2 + R^2 f_0^2)^{-11/6} \, df_u df_v \quad (27)$$

$$Q_1(f_u, f_v) = \frac{J_1(2\pi\sqrt{f_u^2 + f_v^2})}{\pi\sqrt{f_u^2 + f_v^2}} \quad (28)$$

where J_1 is a first order Bessel function. Following the method laid out by Noll, the Q function in the case of piston can be seen in Eq. 28. For the purpose of simplifying, the constants and seeing parameter, r_0, outside the integrals will be defined as β, seen in Eq. 29.

$$\beta(r_0) = 0.022896 \left(\frac{R}{r_0}\right)^{-5/3} \quad (29)$$

The final definition for the variance of piston, defined as σ_p^2, is seen as Eq. 30. This function will not be solved analytically but will be solved numerically using a computer.

$$\sigma_p^2 = \langle a_1^* a_1 \rangle = \beta(r_0) \int\int \left| \frac{J_1(2\pi\sqrt{f_u^2 + f_v^2})}{\pi\sqrt{f_u^2 + f_v^2}} \right|^2 (f_u^2 + f_v^2 + R^2 f_0^2)^{-11/6} \, df_u df_v \quad (30)$$

3.1.2 Numerical Analysis

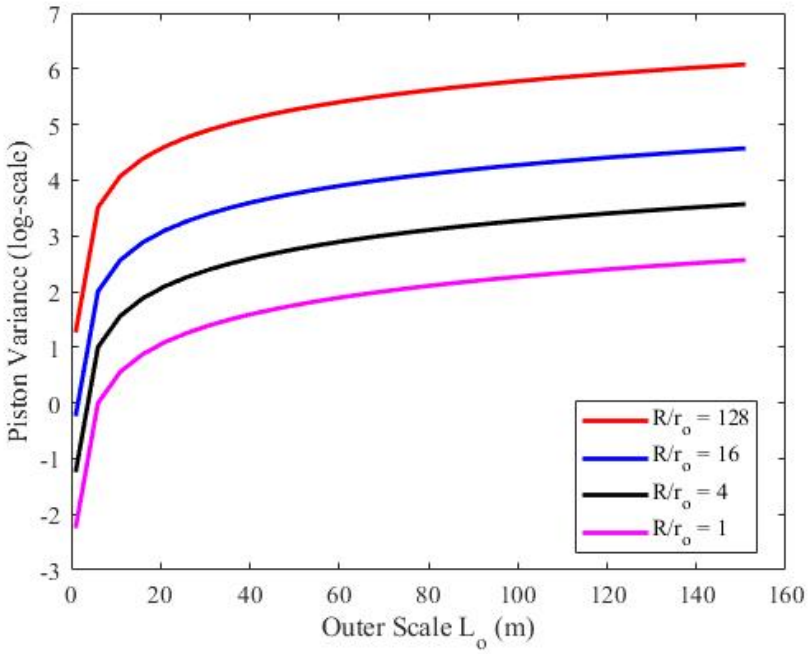

Figure 11: The log-scale of piston variances per outer scale, in meters. Several different ratios of R/r_0 are plotted.

The analysis of Eq. 30 was done using MATLAB. The MATLAB code of this analysis can be found in the appendix. The frequency spectrum was sampled at a rate of $f_s = f_0/2$. As seen by Figure 3.1.2 as the outer scale increases the variance of piston grows quite rapidly. It can also be seen that the variance follows a similar '5/3rds' rule as seen in Noll's work[6]. As with all other Zernike coefficient variances found using von Karman turbulence, Piston variance will approach the Zernike coefficient variance found using Kolmogorov turbulence as outer scale approaches infinity. This means in the case of piston it will approach infinity as outer scale approaches infinity. In practical applications though this does not mean that with a larger outer scale that there will be a larger piston variance. Usually as outer scale increases with less turbulent air so does the seeing parameter. It is important to keep in mind that the two are dependent variables.

3.2 Spatiotemporal Piston Autocovariance

The spatial piston autocovariance, and correlation, of two separate apertures can be solved in a similar fashion as the variance of one aperture. If it is assumed that the two apertures in question are of identical size then the only needed extra input for the spatial autocovariance is the separation, or baseline, of the apertures in both the X and Y-axis. Following the work of Putnam[9] and Conan[10], this separation will be treated as a shift. By applying the Fourier shift theorem to Eq. 30 the spatial autocovariance can be defined as:

$$Cov(a_{1a}, a_{1b}; 0) = \Gamma_{D0} = \beta(r_0) \int\int |Q_1(f_u, f_v)|^2 \left(f_u^2 + f_v^2 + R^2 f_0^2\right)^{-11/6} ... \\ \exp\left(2\pi i R^{-1}(B_x f_u + B_y f_v)\right) df_u df_v \quad (31)$$

where B_x and B_y are the X-axis and Y-axis spatial separation between the center of the apertures, and $i = \sqrt{-1}$. This is referred to as the baseline in interferometry. The value $(1/R)$ in the exponential is a product of the shift and normalization of frequency, it's proof can be seen in appendix A. Of course, in order to find the autocorrelation of the piston coefficients the autocovariance will need to be divided by the piston standard deviation of the two apertures in question.

The same method used in Putnam[9], Cain[23], and Richmond[24] will be used in order to derive the spatiotemporal autocovariance. The spatial shift in the turbulent air caused by wind will be determined by the winds velocity. This spatial shift from the movement in the turbulent air is again applied to Eq. 31 to get the spatiotemporal

autocovariance of piston in the two apertures:

$$Cov(a_{1a}, a_{1b}; \tau) = \Gamma_{D\tau} = \beta(r_0) \int\int |Q_1(f_u, f_v)|^2 \left(f_u^2 + f_v^2 + R^2 f_0^2\right)^{-11/6} ... \\ \exp\left(2\pi i R^{-1}((B_x + v_x\tau)f_u + (B_y + v_y\tau)f_v)\right) df_u df_v \quad (32)$$

where v_x and v_y are wind speeds corresponding the two axes, and τ is the time between the images. Figure 11 shows that as the spatial shift in Eq. 32 increases the piston autocovariance, and hence correlation, decreases in the two apertures. The autocovariance decreases less while the shift is less than the aperture radius length and then more rapidly after the shift increases beyond the radius length. The autocovariance decays at a slower rate as the shift reaches higher lengths but will approach zero as the shift approaches infinity.

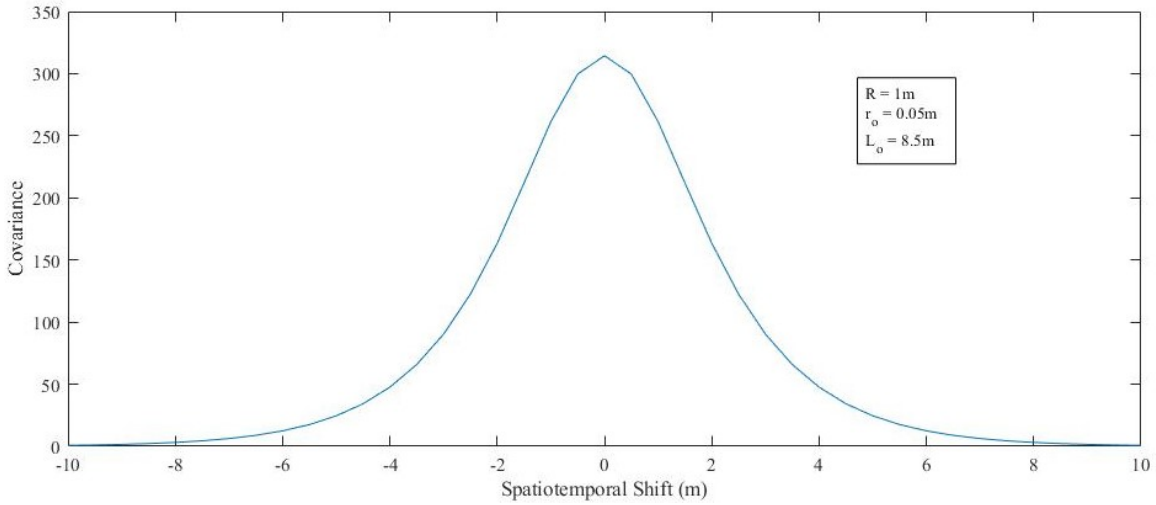

Figure 12: The autocovariance of piston per spatiotemporal shift, in meters. The radius of the apertures were set at 0.5m, r_0 was set at 10cm, and L_0 at 50m

3.3 Tilt Variance and Spatiotemporal Autocovariance

In order to obtain the tilt variance and autocovariance the same method will be used as was used for piston, but the Q-function will be changed to reflect X-tilt, also

known as tip. Y-tilt will have the same results as X-tilt due to it being the same polynomial except the change in the y-axis. Again, the basis for this section will be Eq. 17. Due to j being even, and n and m being 1, the Q-function resolves to Eq. 33 for X-tilt.

$$Q_2(f_u, f_v) = 2i \frac{J_2(2\pi\sqrt{f_u^2 + f_v^2})}{\pi\sqrt{f_u^2 + f_v^2}} \cos(\tan^{-1}(f_u/f_v)) \tag{33}$$

where J_2 is a second order Bessel function. The X-tilt variance and autocovariance can be seen below as Eqs. 34 and 35. The only change in these equations from their piston counterparts is the change in the Q-function. This is due to the Q-function being the Fourier transform of the aperture-Zernike polynomial product.

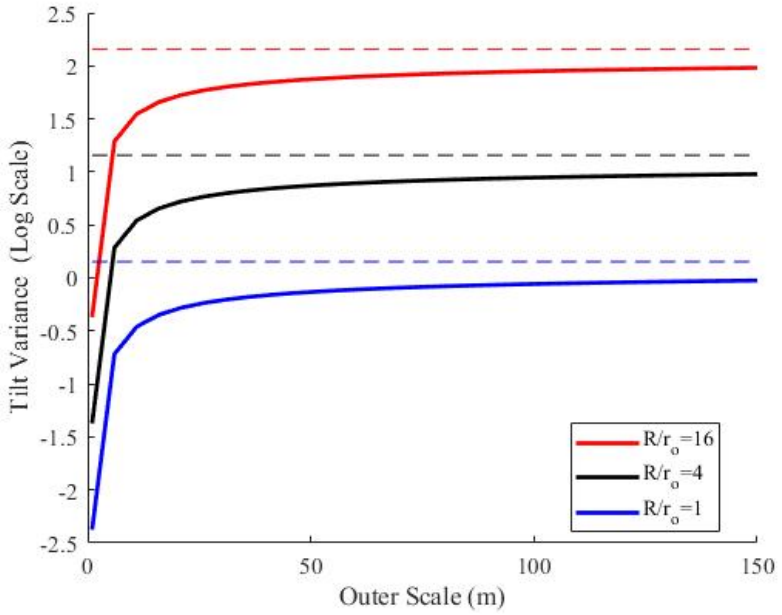

Figure 13: The tilt variance at three different values of R/r_0. The dashed lines of same color are the values of the tilt variance if Kolmogorov PSD is used instead of von Karman PSD.

$$\langle a_2^* a_2 \rangle = \beta(r_0) \int\int |Q_2(f_u, f_v)|^2 \left(f_u^2 + f_v^2 + R^2 f_0^2\right)^{-11/6} df_u df_v \tag{34}$$

$$Cov(a_{2a}, a_{2b}; \tau) = \beta(r_0) \int\int |Q_2(f_u, f_v)|^2 \left(f_u^2 + f_v^2 + R^2 f_0^2\right)^{-11/6} ...$$
$$\exp\left(2\pi i R^{-1}((B_x + v_x\tau)f_u + (B_y + v_y\tau)f_v)\right) df_u df_v \quad (35)$$

As expected, numerical analysis shows the tilt variance approaching the tilt variance determined by Noll as the outer scale approaches infinity. Figure 13 shows this at several different R/ro values. This is expected because the von Karman PSD approaches Kolmogorov PSD as the outer scale increases in value. As seen in Figure 14 the spatiotemporal autocovariance acts as expected as the magnitude of the spatiotemporal shift increases. There is a noticeable difference between the autocovariance of the piston and tilt. The piston remains more correlated than tilt as the shift increases. This means at any baselines for interferometers piston will have a higher autocorrelation than any Zernike coefficient and X-tilt and Y-tilt will have the second highest. The same can be said for higher wind speeds or longer delay between image capture. This pattern follows the work of Noll[6]. As the order of the Zernike polynomial grows the autocovariance will start to resemble a Dirac delta function more.

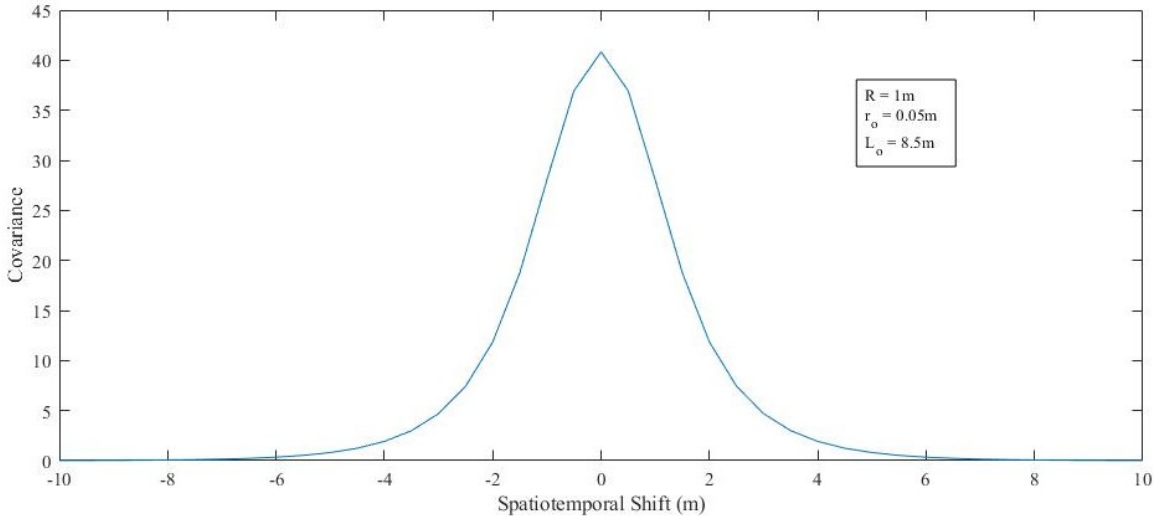

Figure 14: The autocovariance of tilt per spatiotemporal shift, in meters. The radius of the apertures were set at 0.5m, r_0 was set at 10cm, and L_0 at 50m

3.4 Piston Tracking with Fringe Tracking

Fringe tracking, as mentioned in 2.6.3, is used to partially correct for optical path difference in interferometers. This section will describe how to model and implement piston differential into a fringe tracker, in this case a group delay tracker. Instead of setting path delay to the previously recorded path delay, as described in 2.6.3, two piston states will be estimated and tracked using a Kalman Filter. Group delay tracking will give the updates to the Kalman Filter. This use of Kalman filtering using Zernike pistons as states has been termed piston tracking.

3.4.1 State Definition

The states will be the piston Zernikes of the two aperture interferometer. This state vector is defined as:

$$\vec{a} = \begin{bmatrix} a_{1a} \\ a_{1b} \end{bmatrix} \tag{36}$$

The first step in defining a stochastic model is to define the mean and covariance of the states. Again, in this case the states are the piston coefficients of the two apertures making up the interferometer. The mean of piston is assumed zero and the covariance matrix of two pistons can be seen in Eq. 38. It should be noted that while the mean of atmospherically introduced piston is zero the mean of piston could not necessarily always be zero; the physical set up of an interferometer could cause some mean path difference.

$$\vec{\mu}_a = \begin{bmatrix} 0 \\ 0 \end{bmatrix} \tag{37}$$

$$\mathbf{\Gamma_a}(a_{1a}, a_{1b}; 0) = \begin{bmatrix} \sigma_p^2 & \Gamma_{D0} \\ \Gamma_{D0} & \sigma_p^2 \end{bmatrix} \tag{38}$$

where again, Γ_{D0} is the piston spatial covariance or $Cov(a_{1a}, a_{1b}; 0)$, and σ_p^2 is the variance of piston.

3.4.2 Conditional Mean and Covariance of the States

The next step in deriving the stochastic model is to define how states evolve temporally, or the temporal relationship they have with one another. To do this the conditional means and covariances of pistons at t_k given to the two previous pistons at time t_{k-1} will be needed. The conditional mean and covariance of the piston in aperture 'a' at time t_k is defined as:

$$\hat{\mu}(t_k) = E[a_{1a}(t_k) \mid \vec{a}(t_{k-1}) = \vec{\mathfrak{a}}] \tag{39}$$

$$\hat{\sigma}^2(t_k) = E[(a_{1a}(t_k) - \hat{\mu}_a(t_k))^2 \mid \vec{a}(t_{k-1}) = \vec{\mathfrak{a}}] \tag{40}$$

where $\vec{a}$ is a vector of realizations of the two piston states. This conditional mean and covariance can be found first by defining a vector of all three random variables $a_{1a}(t_k)$, $a_{1a}(t_{k-1})$, and $a_{1b}(t_{k-1})$, then partitioning off the vector and its respectful covariance matrix with respect to $a_{1a}(t_k)$ which can be seen as:

$$\left[\begin{array}{c} a_{1a}(t_k) \\ a_{1b}(t_k) \\ \hline a_{1a}(t_{k-1}) \\ a_{1b}(t_{k-1}) \end{array}\right] \tag{41}$$

$$\left[\begin{array}{cc|cc} \sigma_p^2 & \Gamma_{D0} & \Gamma_{0\tau} & \Gamma_{D\tau} \\ \Gamma_{D0} & \sigma_p^2 & \Gamma_{D\tau} & \Gamma_{0\tau} \\ \hline \Gamma_{0\tau} & \Gamma_{D\tau} & \sigma_p^2 & \Gamma_{D0} \\ \Gamma_{D\tau} & \Gamma_{0\tau} & \Gamma_{D0} & \sigma_p^2 \end{array}\right] \tag{42}$$

where $\Gamma_{0\tau}$ is the temporal covariance of piston or $Cov(a_{1a}, a_{1a}; \tau)$, which is the covariance between $a_{1a}(t_k)$ and $a_{1a}(t_{k\mp1})$. The value $\Gamma_{D\tau}$ is spatiotemporal covariance or $Cov(a_{1a}, a_{1b}; \tau)$, and is the covariance between $a_{1a}(t_k)$ and $a_{1b}(t_{k\mp1})$. This method is described in "Multivariate Statistics: a Vector Space Approach" [25] and is used to find conditional mean and covariance for random vectors following a multivariate normal distribution. More can be read about this vector space approach in appendix A. This vector space approach for finding the conditional mean and variance yields the following for the conditional mean:

$$\hat{\mu}(t_k) = \begin{bmatrix} \Gamma_{0\tau} & \Gamma_{D\tau} \\ \Gamma_{D\tau} & \Gamma_{0\tau} \end{bmatrix} \begin{bmatrix} \sigma_p^2 & \Gamma_{D0} \\ \Gamma_{D0} & \sigma_p^2 \end{bmatrix}^{-1} \begin{bmatrix} \mathfrak{a}_{1a} \\ \mathfrak{a}_{1b} \end{bmatrix} \tag{43}$$

where the superscript on the middle matrix stands for taking the inverse, and the values $\mathfrak{a}_{1a}$ and $\mathfrak{a}_{1b}$ are the realizations of a_{1a} and a_{1b} at t_{k-1}. Solving this will give:

$$\hat{\mu}(t_k) = \frac{1}{\sigma_p^4 - \Gamma_{D0}^2} \begin{bmatrix} (\Gamma_{0\tau}\sigma_p^2 - \Gamma_{D\tau}\Gamma_{D0})\mathfrak{a}_{1a} + (\Gamma_{D\tau}\sigma_p^2 - \Gamma_{0\tau}\Gamma_{D0})\mathfrak{a}_{1b} \\ (\Gamma_{D\tau}\sigma_p^2 - \Gamma_{0\tau}\Gamma_{D0})\mathfrak{a}_{1a} + (\Gamma_{0\tau}\sigma_p^2 - \Gamma_{D\tau}\Gamma_{D0})\mathfrak{a}_{1b} \end{bmatrix} \tag{44}$$

The conditional covariance following a state vector approach is first written as:

$$\hat{\sigma}^{\mathbf{2}}(t_k) = \begin{bmatrix} \sigma_p^2 & \Gamma_{D0} \\ \Gamma_{D0} & \sigma_p^2 \end{bmatrix} - \begin{bmatrix} \Gamma_{0\tau} & \Gamma_{D\tau} \\ \Gamma_{D\tau} & \Gamma_{0\tau} \end{bmatrix} \begin{bmatrix} \sigma_p^2 & \Gamma_{D0} \\ \Gamma_{D0} & \sigma_p^2 \end{bmatrix}^{-1} \begin{bmatrix} \Gamma_{0\tau} & \Gamma_{D\tau} \\ \Gamma_{D\tau} & \Gamma_{0\tau} \end{bmatrix} \tag{45}$$

This can be written as:

$$\hat{\sigma}^{\mathbf{2}}(t_k) = \begin{bmatrix} \sigma_p^2 - \frac{\Gamma_{0\tau}\sigma_p^2 - \Gamma_{D\tau}\Gamma_{D0}}{\sigma_p^4 - \Gamma_{D0}^2}\Gamma_{0\tau} - \frac{\Gamma_{D\tau}\sigma_p^2 - \Gamma_{0\tau}\Gamma_{D0}}{\sigma_p^4 - \Gamma_{D0}^2}\Gamma_{D\tau} \\ \Gamma_{D0} - \frac{\Gamma_{0\tau}\sigma_p^2 - \Gamma_{D\tau}\Gamma_{D0}}{\sigma_p^4 - \Gamma_{D0}^2}\Gamma_{D\tau} - \frac{\Gamma_{D\tau}\sigma_p^2 - \Gamma_{0\tau}\Gamma_{D0}}{\sigma_p^4 - \Gamma_{D0}^2}\Gamma_{0\tau} \end{bmatrix} \tag{46}$$

For the purpose of simplicity the following will be defined:

$$\hat{\sigma}_1^2 = \sigma_p^2 - \frac{\Gamma_{0\tau}\sigma_p^2 - \Gamma_{D\tau}\Gamma_{D0}}{\sigma_p^4 - \Gamma_{D0}^2}\Gamma_{0\tau} - \frac{\Gamma_{D\tau}\sigma_p^2 - \Gamma_{0\tau}\Gamma_{D0}}{\sigma_p^4 - \Gamma_{D0}^2}\Gamma_{D\tau} \tag{47}$$

$$\hat{\sigma}_2^2 = \Gamma_{D0} - \frac{\Gamma_{0\tau}\sigma_p^2 - \Gamma_{D\tau}\Gamma_{D0}}{\sigma_p^4 - \Gamma_{D0}^2}\Gamma_{D\tau} - \frac{\Gamma_{D\tau}\sigma_p^2 - \Gamma_{0\tau}\Gamma_{D0}}{\sigma_p^4 - \Gamma_{D0}^2}\Gamma_{0\tau} \tag{48}$$

3.4.3 Stochastic Model

Finally, with the conditional means and variances solved for the stochastic model may be completed. Following the general format of a Kalman filter the stochastic model will be in the form:

$$\vec{a}(t_k) = \hat{\mathbf{\Phi}}\vec{a}(t_{k-1}) + \mathbf{B}_d\vec{u}(t_{k-1}) + \vec{w}_d(t_{k-1}) \tag{49}$$

where $\hat{\mathbf{\Phi}}$ is a state transition matrix, or the temporal relationship between the states. The value $\mathbf{B}_d\vec{u}(t_{k-1})$ is an input vector. This will be ignored for the time being but if the path delay is adjusted this is the proper place to add piston input. The vector $\vec{w}_d(t_{k-1})$ is the variance added to the states every transition and is traditionally called the state noise vector because it is defined as additive white Gaussian noise (AWGN). The Cholesky decomposition of the covariance of this noise vector is required to simulate the states over time so the covariance is defined as:

$$\mathbf{Q}_d = E[\vec{w}_d\vec{w}_d^T] \tag{50}$$

The output, in this case the piston differential, will be defined as:

$$z(t_k) = \mathbf{H}\vec{a}(t_k) + \vec{v}(t_k) \tag{51}$$

where z is the output, $\mathbf{H}$ is the relationship between the states and the output, and $\vec{v}$ is output noise which will be ignored for this purpose of this paper but this is where servo error and variance in group delay estimation may be added. In summary, the new states will be equal to something of the old states plus noise, and possibly some input. With the form of the model explained, the following is the definition of the model:

$$\hat{\mathbf{\Phi}} = \begin{bmatrix} \frac{\Gamma_{0\tau}\sigma_p^2 - \Gamma_{D\tau}\Gamma_{D0}}{\sigma_p^4 - \Gamma_{D0}^2} & \frac{\Gamma_{D\tau}\sigma_p^2 - \Gamma_{0\tau}\Gamma_{D0}}{\sigma_p^4 - \Gamma_{D0}^2} \\ \frac{\Gamma_{D\tau}\sigma_p^2 - \Gamma_{0\tau}\Gamma_{D0}}{\sigma_p^4 - \Gamma_{D0}^2} & \frac{\Gamma_{0\tau}\sigma_p^2 - \Gamma_{D\tau}\Gamma_{D0}}{\sigma_p^4 - \Gamma_{D0}^2} \end{bmatrix} \tag{52}$$

$$\mathbf{Q}_d = \begin{bmatrix} \hat{\sigma}_1^2 & \hat{\sigma}_2^2 \\ \hat{\sigma}_2^2 & \hat{\sigma}_1^2 \end{bmatrix} \tag{53}$$

$$\mathbf{H} = \begin{bmatrix} \frac{\lambda_0}{2\pi} & \frac{-\lambda_0}{2\pi} \end{bmatrix} \tag{54}$$

This stochastic model will be used to both simulate data and to Kalman filter piston states during group delay estimation. This is done by propagating these states through time steps, updating them with OPD obtained from fringe tracking. Eq.55 shows the conditional mean of the pistons given previous measurements and Eq.57 shows the conditional covariance of the pistons given previous measurements. These will be used to propagate the states forward through time steps. Eq.58 shows the conditional mean of the pistons given previous and current measurements and Eq.59 shows the conditional covariance of the pistons given previous and current measurements. These will be used to update the states after a measurement.

$$\hat{a}^-(t_k) = \hat{\mathbf{\Phi}}\hat{a}^+(t_{k-1}) \tag{55}$$

If there is a wish to simulate pistons the looping algorithm would be:

$$\hat{a}^{-}(t_k) = \hat{\mathbf{\Phi}}\hat{a}^{+}(t_{k-1}) + Chol(\mathbf{Q}_d) \begin{bmatrix} \mathcal{N}(0,1) \\ \mathcal{N}(0,1) \end{bmatrix} \tag{56}$$

where $Chol(\mathbf{Q}_d)$ is taking the Cholesky decomposition of $\mathbf{Q}_d$ and is only added when simulating data to add variance to the states. The function $\mathcal{N}(0,1)$ is a normal random variable with a mean of zero and unit variance.

$$\hat{\mathbf{\Gamma}_a}^{-}(t_k) = \hat{\mathbf{\Phi}}\hat{\mathbf{\Gamma}_a}^{+}(t_{k-1})\hat{\mathbf{\Phi}}^T + \mathbf{Q}_d \tag{57}$$

where the superscript T denotes the transpose. The update conditional mean and covariance are:

$$\hat{a}^{+}(t_k) = \hat{a}^{-}(t_k) + \hat{\mathbf{\Gamma}_a}^{-}(t_k)\mathbf{H}^T[\mathbf{H}\hat{\mathbf{\Gamma}_a}^{-}(t_k)\mathbf{H}^T]^{-1}[z(t_k) - \mathbf{H}\hat{a}^{-}(t_k)] \tag{58}$$

$$\hat{\mathbf{\Gamma}_a}^{+}(t_k) = \hat{\mathbf{\Gamma}_a}^{-}(t_k) - \hat{\mathbf{\Gamma}_a}^{-}(t_k)\mathbf{H}^T[\mathbf{H}\hat{\mathbf{\Gamma}_a}^{-}(t_k)\mathbf{H}^T]^{-1}\mathbf{H}\hat{\mathbf{\Gamma}_a}^{-}(t_k) \tag{59}$$

These equations follow traditional Kalman filtering practices. The simulations derived from this model will be discussed in Chapter IV.

3.5 Data Collection

In order to verify the results of this model an experimentation was arranged. The main purpose of the experiment is to verify piston autocovariance. In order to get path error data to do this verification, fringes must be formed and fringe jitter will be collected over time. In order to fluctuate path error the light must pass through turbulent air. This brings up the need to estimate the seeing parameter and outer scale of the turbulent air. To do this the light source will be split, the jitter of the

two beams will be correlated to tilt, and those tilt variances and the tilts' covariance will in turn be used to estimate the seeing parameter and outer scale using the tilt autocovariance function.

3.5.1 Lab Set Up

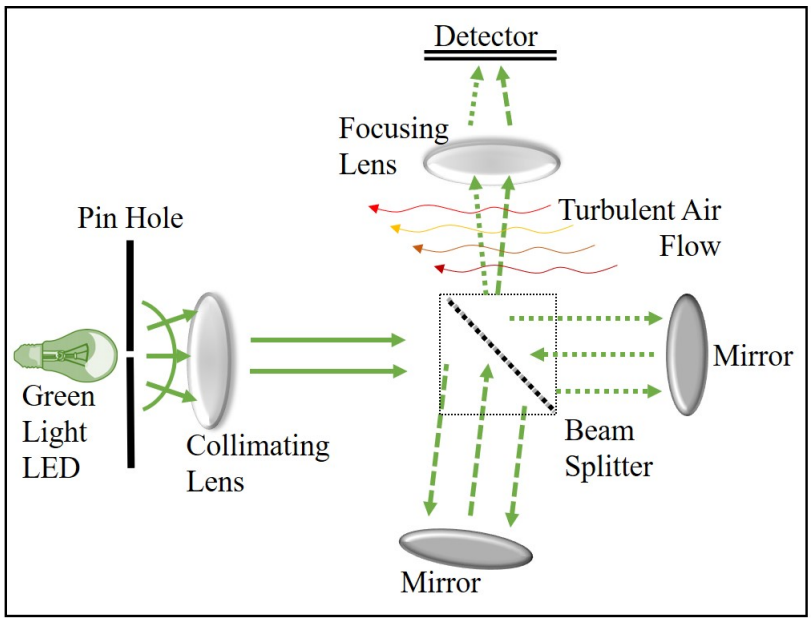

Figure 15: A graphic showing the rudimentary layout of the optical set up for collecting tilt and fringe data.

The experiment layout will now be described starting from the source and ending with the detector. The source being used is a LED with a bandwidth of about $490nm$ to $550nm$ with a mean wavelength of $530nm$. The spectrum being used in future simulations and estimations can be seen in Figure 16. There is a pin hole aperture of $30\mu m$ in front of the source. The light then passes through a collimating lens and travels to a beam splitter. The two beams then reflect off mirrors and travel to a focusing lens which focuses the light to the detector. The focal length of the lens is $0.2m$ and the detector sampling is $5.5\mu m$. The turbulent air heat source is located to the right of the focusing lens and is situated so the air flows in-front of the lens

as depicted in Figure 15. The detector integration time needed is set low enough so a frozen flow assumption could be made about the turbulence. An integration time between $20ms$ to $40ms$ was used. Images were collected at one image per second.

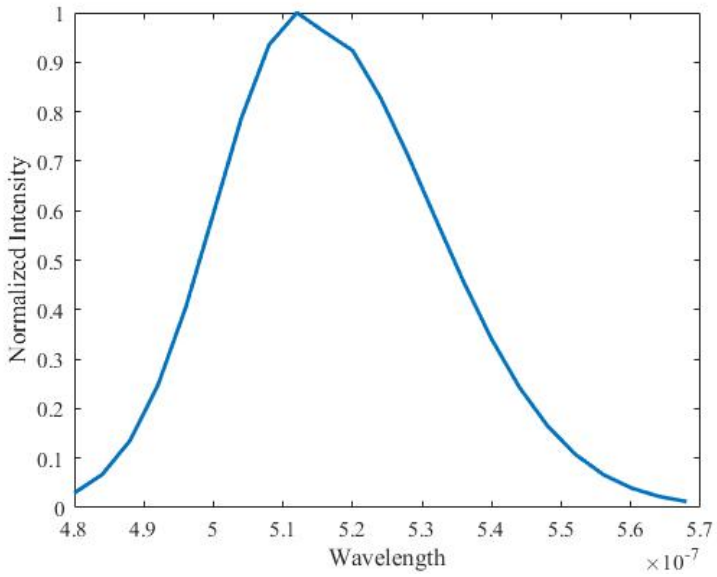

Figure 16: Spectrum of source used in data collection

When collecting fringe jitter data a two hole aperture mask will be placed directly in-front of the focusing lens. The two apertures of the mask will have a diameter of $2.779mm$ with a separation of $2.3mm$. This will cause two fringe patterns two be formed at the detector. If only one fringe pattern is desired a mirror is blocked. In order to get path error data from this fringe data more post processing needs to be done. The point source, while being very small, is not ideal and has some width to it. The source will have to be deconvolved with the image. An example of a fringe pattern formed in this manner can be seen by Figure 17. Then the fringe patterns will have to be correlated to simulated fringes to determine path difference. Visibility of the fringes was not used to determine path difference due to poor quality of the signal to noise ratio(SNR) and the absence of enough frequency information do correctly determine visibility. The poor SNR kept visibility measurements from being accurate enough

to deduce an accurate enough path difference. To deduce the visibility from the frequency information of the fringes one needs more that three fringes to accurately do so. Unfortunately the poor SNR hides two lower intense fringes from appearing in the images. When collecting image jitter apertures are placed in-front of the mirrors

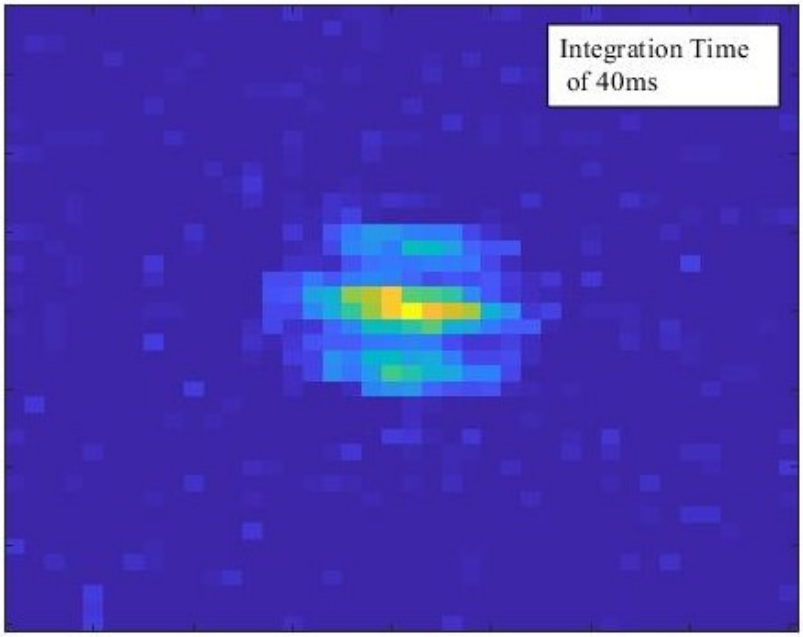

Figure 17: Recorded fringe pattern using the optical system created for fringe, or path error, data collection.

which limits and shapes the light arriving at the focusing lens. The image formed in this manner can be seen in Figure 18

3.5.2 Estimation of Seeing and Outer Scale

Once jitter data is collected it will be transformed to tilt data by scaling the data by a constant. The constant is the amount of tilt is needed to move the image center one pixel. With this scalar the amount of pixels off center the image is can be translated to amount of tilt seen in the image. The tilt variance of this data and the spatial covariance of the two tilts are then found.

The results of this data are then compared to a mapping of variance and covariance

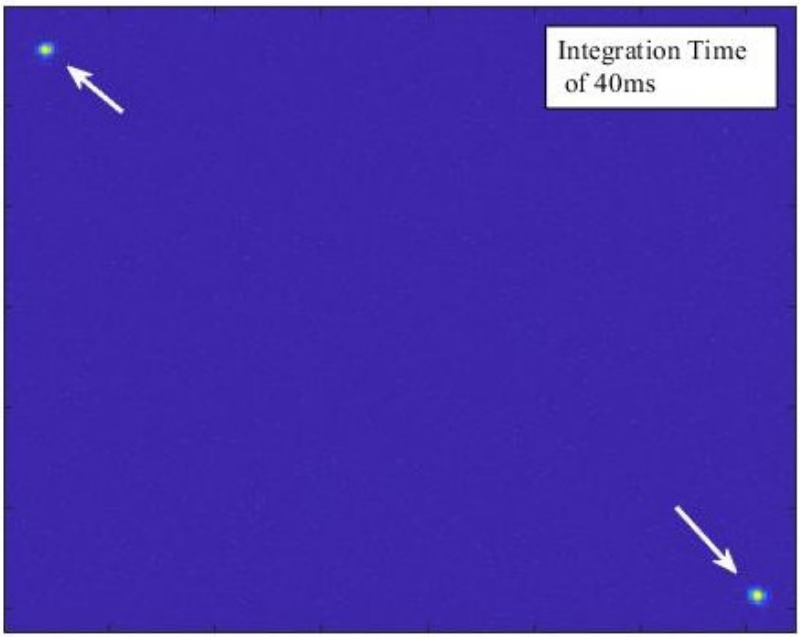

Figure 18: Recorded 'dots' using the optical system described for the use of determining atmospheric parameters. The arrows on the figure are marking the location of the dots who's source is the same but travel different optical paths.

generated by varying seeing parameters and outer scales. The seeing parameter and outer scale that generates a tilt variance and spatial covariance most similar to that recorded will be chosen for the turbulence. These atmospheric parameters will be used to generate a piston variance and spatial covariance, which in turn will be used to determine what the expected path length error variance will be.

3.6 Summary of Methodology

This chapter described the piston variance and spatiotemporal autocovariance with a von Karman phase PSD. As discussed in Chapter 2, others have calculated path error variance before but not with a von Karman PSD. They instead used other non-Kolmogorov power spectral densities or other methods. It is my opinion that other PSDs are used because they may be more accurate and can be used to achieve closed-form expressions for Zernike coefficient covariance. This chapter describes

solving this complex integral numerically and discretely vis-a-vie a computer. Tilt variance and spatiotemporal autocovariance is then described due to it's use in data collection. This tilt model is similar to the Angle-of-Arrival model discussed in section 2.4. The method of collecting that tilt and path error data was then discussed. The results of simulation using this piston model and the data collected will be described in the next chapter.

IV. Results and Analysis

4.1 Results of Simulations

There were in total 3 different simulations performed. The first was a Monte Carlo of piston without temporal correlation. Then temporal correlation was added to the second of the simulations. The parameters of the lab set up described in the previous chapter were used in these first two experiments. The parameters were then modified, and using the temporal piston model, data was generated for use in simulating the Kalman filter and the fringe tracking performance.

4.1.1 Piston Monte Carlo Simulation with No Temporal Correlation

The first simulation done was a non-temporally correlated piston. That simulation was a Monte Carlo Simulation and was done by generating bivariate random numbers with covariance equal to Eq. 38. The piston variance in this instance was 1.773 and the spatial correlation was 0.7373. This was done 125 times to generate a string of non-temporally correlated pistons. There were 10,000 trials in the Monte Carlo simulation. Figure 19 shows just one trial of piston and path error data generated. The piston coefficients fluctuated widely throughout time. Although piston fluctuated widely throughout time the two stayed closely correlated. This leads to the path error having a variance close to $\mathbf{2.4x10^{-15}}m^2$.

4.1.2 Piston Monte Carlo Simulation with Temporal Correlation

Temporal correlation was then added and a Monte Carlo simulation using the algorithm described in section 3.4.3 was implemented. There were 10,000 trials done. Figure 20 shows just one trial of piston and path error data. As observed in the figure, the pistons stay well correlated and there are no major fluctuations over time because

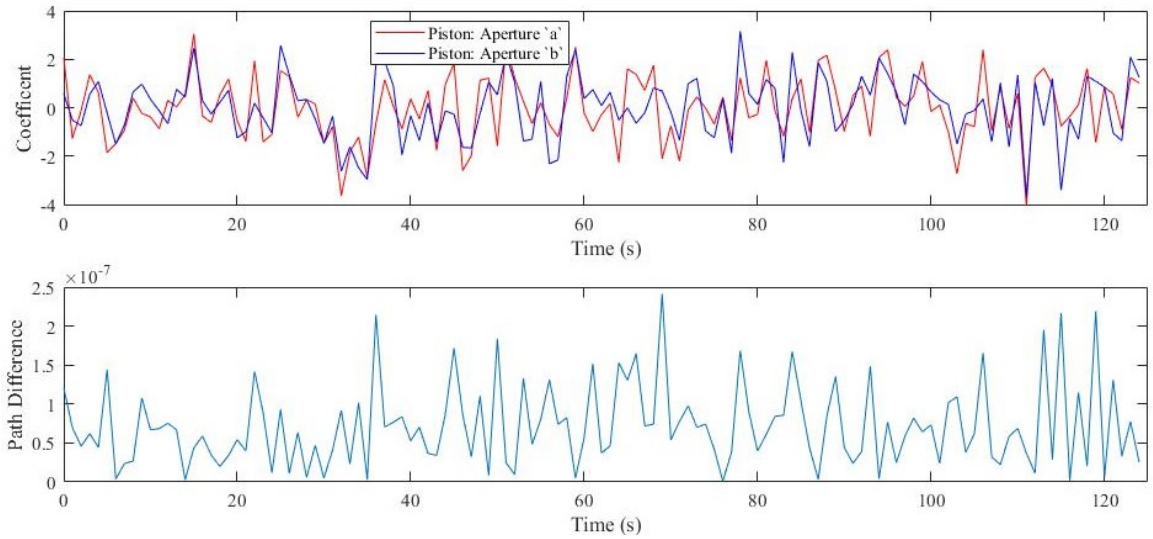

Figure 19: Piston coefficients with no temporal correlation (top) and the corresponding path error (bottom) in meters from those coefficients. The delay period used was 1 second. All other system parameters matched that of the experimental setup described in section 3.5.1 with $L_0 = 0.05m$ and $r_0 = 0.0079m$.

of the temporal correlation. This shows that after a full second between image capture the coefficients are not very correlated. In fact the estimated temporal correlation between the same aperture is 0.0004 and a temporal correlation for differing apertures of 0.0003. These temporal correlations were found using a X-coordinate wind speed of $0.1m/s$ and a Y of $0.05m/s$. These are estimates for wind speed but the point is to prove that even with wind speed estimates and a delay of $1s$ that temporal correlation is low. The path error fluctuates at a variance of at $\mathbf{2.4x10^{-15}}m^2$ which matches when no temporal correlation was considered. A this variance the maximum path error stays well under a micrometer. The coherence length of the source light is $8\mu m$. With this in mind the fringes in the experimental data collection should remain apparent throughout time.

There was an interest to find when the temporal correlation reaches to a point of 0.5. This is because a strong temporal correlation would be needed if there is future interest in analyzing temporal effects. By simulation, it was found that the time delay

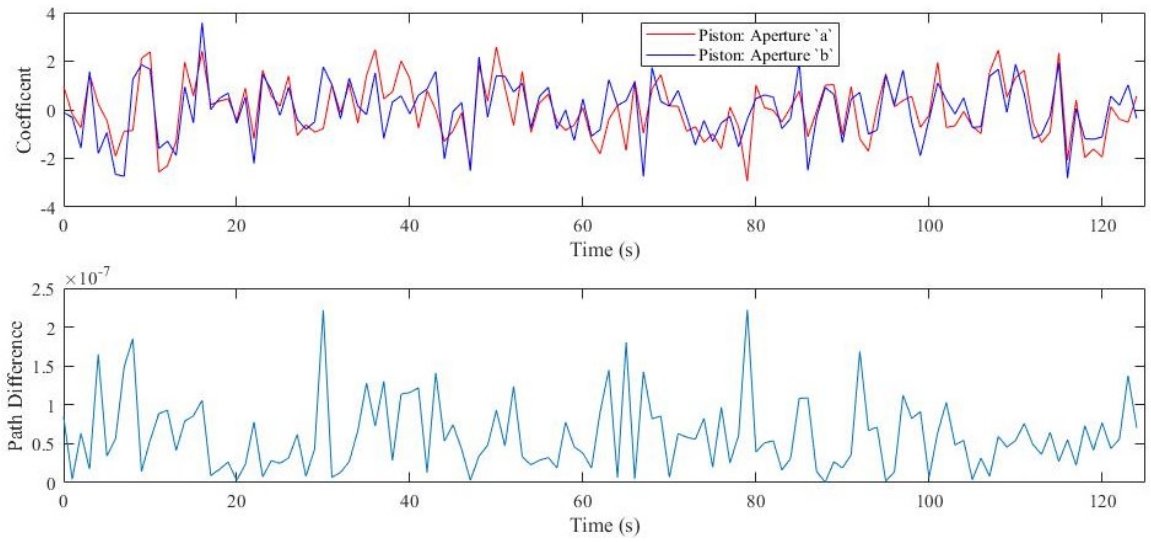

Figure 20: Piston coefficients with temporal correlation (top) and the corresponding path error (bottom) in meters from those coefficients. The delay period used was 1 second. All other system parameters matched that of the experimental setup described in section 3.5.1 with $L_0 = 0.05m$ and $r_0 = 0.0079m$.

that gives a temporal correlation of 0.5 was found to be $0.08s$. The temporal correlation at $20ms$ and $40ms$ are 0.9233 and 0.7795 respectfully. This is important to note because those are the two different integration times used during data collection. The very small integration time is needed for the frozen flow turbulence assumption made during image capture. Completely frozen turbulence will have a temporal correlation very near 1.

4.1.3 Fringe Tracking Performance

The Kalman filter developed was used to supplement a group delay fringe tracker in simulation. This was done using a fringe pattern simulation created at AFIT by another graduate student and faculty, and the path error data generated by the piston simulation model with temporal correlation. The parameters of the simulation were: $R = 0.125m$, $B_x = 2.5m$, $B_y = 0m$, $\tau = 0.1$, $v_x = 1m/s$, $v_y = 1m/s$, $L_0 = 8.5m$, and $r_0 = 5cm$. These parameters led to a piston variance of 441, spatial correlation of

0.2714, a temporal correlation of 0.9825, a spatiotemporal correlation of 0.2543 and a path error variance of $8.1\mathbf{x}10^{-14}m^2$. A performance comparison was done with the Kalman filter and without the filter. A green light source was used for the fringe simulation. Figure 21 shows a realization of the visibility for three different cases: group delay with piston tracking, group delay only, and no fringe tracking. When

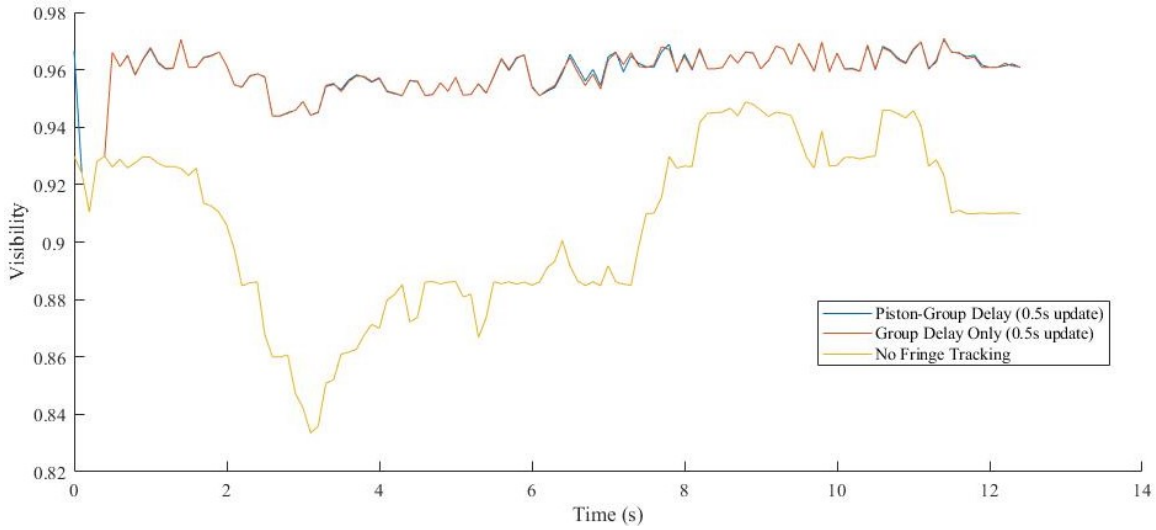

Figure 21: The visibility over time of group delay with piston tracking, group delay only, and no fringe tracking. Path error data used was generated.

group delay is implemented the visibility improves drastically. Just from observing the figure though it doesn't appear that adding piston tracking improved the situation. In reality, the average visibility with piston tracking is slightly higher than only group delay fringe tracking. Table 3 shows the mean visibility and variance for a 100 trial Monte Carlo simulation. Out of the 100 trials, 85 of them have better or equal visibility with piston tracking. The variance for piston tracking-group delay is also lower than without piston tracking. This can be important in the implementation of a delay path to correct for path error. The lower variance helps the servo of the delay path adjust to the needed position faster. Most of the time the variance is lower with piston tracking; 90 of the 100 trials had lower variance with piston tracking. The piston tracker will improve the visibility and lower variance variably with different

interferometer and atmospheric parameters.

Table 3: Fringe tracking performance showing a comparison between no fringe tracking, group delay, and group delay with piston tracking

	Mean Visibility	Variance
No Fringe Tracking	0.8500	$6.95\text{x}10^{-4}$
Group Delay Only	0.9197	$2.32\text{x}10^{-3}$
Piston-Group Delay	0.9205	$2.15\text{x}10^{-3}$

4.2 Results of Data Collection

In order to prove the validity of the piston correlation model the experiment described in section 3.5.1 was implemented. To reiterate, tilt data was first collected to estimate the atmospheric parameters of outer scale and seeing parameter. Fringe patterns were then formed and collected to estimate path difference. Using the outer scale and seeing parameter estimated from the tilt data, a theorized path error variance can be generated and compared to the path error variance collected by the fringe patterns.

4.2.1 Tilt Correlation and Atmospheric Parameters

The tilt data was collected using the lab set up discussed in section 3.5.1. Once image motion was collected, the center of the two images per each frame was calculated. The amount of pixel movement from the mean center is proportional to the amount Zernike tilt. The proportion of pixel movement to Zernike tilt was calculated by modeling the optical system. This process is how the X-tilt and Y-tilt of each image was calculated per frame. Figure 22 shows the first 125 X and Y-tilts coefficient values for the two images captured. From the X-tilt variance and correlation values collected the atmospheric parameters were estimated. This was done by first mapping out values of X-tilt variance and spatial covariance using different values of

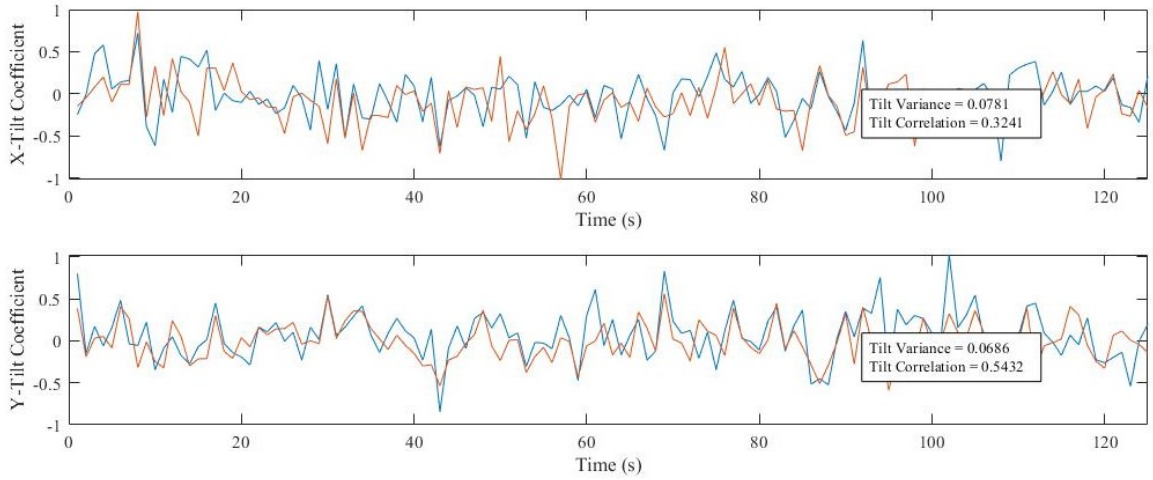

Figure 22: The X and Y-tilt data for the first 125 image captures. X-tilt variance of 0.0781 and correlation of 0.3241, Y-tilt of 0.0686 and correlation of 0.5432 were collected

outer scale and seeing parameter. Then the nearest matching variance and spatial covariance was chosen. Table 4 shows a comparison between the recorded and chosen tilt variance and spatial correlation.

Table 4: A comparison of tilt covariance data and chosen covariance for parameter estimation

	Variance	Spatial Correlation
Recorded	0.0781	0.3241
Chosen	0.0777	0.3173

The outer scale corresponding to this tilt variance and spatial covariance is $L_0 = 0.05m$ and a seeing parameter of $r_0 = 0.79cm$. This is very poor atmospheric seeing quality but poor quality seeing was expected because warm air is being generated and blown across the apertures in an air conditioned environment.

4.2.2 Piston Fringe Data

The fringe data was generated by using the lab set up described in section 3.5.1. After fringes were captured each image needed to have the source deconvolved with it as described in section 3.5. This source deconvolution made the fringes more

prevalent. The fringes were then correlated to simulated fringe patterns set at a range of differing path errors. Once a fringe pattern match was determined the path error was known. It should be noted that this process was not the original process to determine path error and the Fourier visibility was originally going to used to estimate path error. Problems arose during the implementation due to the low number of visible fringes; lower intensity fringes were hidden by low signal to noise ratio (SNR). Figure 23 shows the collected path error per frame of 125 frames. Two fringe patterns were collect per frame and fringe patterns were recorded at $20ms$, $30ms$, and $40ms$ integration times. SNR is naturally higher at the $40ms$ integration time but the frozen flow assumption holds less. The vice versa can be said about the $20ms$ integration time. Another matter to note is that there was some visible error

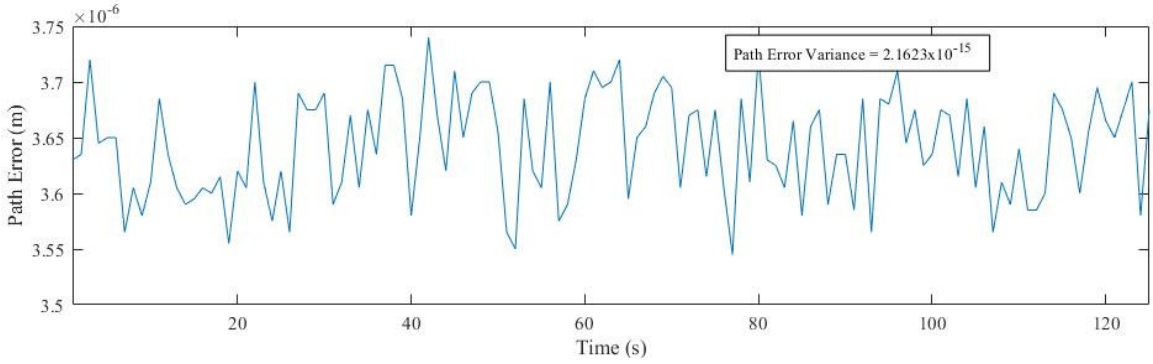

Figure 23: Path error data collected at $40ms$ integration time. The variance for this 125 frame data set was $2.16\mathbf{x}10^{-15}m$

when correlating the captured fringe patterns to simulated patterns. The error was slight and only occurred in about half a dozen of the 125 frames but may have led to some error in estimating the path error variance. The mean path error variance recorded was $\mathbf{2.34x10^{-15}}m^2$; this is the mean of the six recorded realizations. The mean path error in this case is near $3.627um$. The reason for the mean path error being so high is piston aberration in the optical set up. The aperture mask simply was not laid completely flat on the focusing lens.

4.3 Comparisons

The results of the experiment compared to that of the simulation are promising. In review, the simulation gave a path error variance near that of $\mathbf{2.4x10^{-15}}m^2$ and the recorded results gave a path error variance of $\mathbf{2.34x10^{-15}}m^2$. Considering that the recorded variance maybe slightly off due to the error of the path error estimation, it might be closer to $2.4\mathbf{x}10^{-15}m^2$ than recorded. There might also be error in estimating the atmospheric parameters or other error cause by other steps in the data collection process. The percent error of the recorded variance to that of the theoretical path error variance was 2.6%

4.4 Summary of Results

The over all results show that this model can be used to simulate Zernike piston and path error variance with a low degree of error. Also, that atmospherically induced Zernike piston remains temporally correlated within an integration time needed for a frozen flow assumption. This demonstrated that pistons of a multi-aperture optical system like an interferometer are highly spatially correlated when the baseline is small and less correlated when the baseline is quite large compared to the radius of the apertures. This larger baseline will cause quite large path error variances which is what makes large baseline stellar interferometry so difficult. This piston model can be looped for use as a Kalman filter which can aid in fringe tracking purposes. The trade off between baseline, aperture size, and system cost and complexity is a vital one. By using this Zernike piston model the ability to accurately predict what interferometers will see will add in this trade off analysis.

V. Conclusions

5.1 Summary of Research

It was hypothesized that the Zernike coefficient statistics for the atmosphere above multi-aperture optical systems can be used for simulation of turbulence effects, especially fringe variance, and for measuring atmospheric turbulence parameters. The methodology taken to prove this hypothesis lead to the statistical models for Zernike piston and tilt using von Karman turbulence. The statistical models were functions of the atmospheric parameters r_0 and L_0. These models were derived from the combination of verified research of others. These statistical models were then used to produce simulated results. These simulations were compared to empirical data to show that they can in fact produce natural analogous results. This proves that the hypothesis does have merit. In the process of verifying the hypothesis the first three research goals were completed. The last research goal of exploring possible uses for this model was reached by showing the benefit of including Kalman filter estimation into fringe tracking. With the hypothesis verified and research goals completed the problem first defined in the introduction is closer to resolution.

5.2 Recommendations and Future Work

If in the future this work is to be continued there are several avenues that should be explored to better the research done and advance it. The following could be done:

1. Due to time constraints, an in depth comparison between the accuracy of the atmospheric parameters produced by this model, and the model used by a DIMM or GSM, was not accomplished and should be done.

2. There should also be a comparison done between this piston differential model

and other models developed.

3. In order to reduce the error in the recorded data a more intense source could be used. A more intense source could better the SNR and make the weaker fourth and fifth fringes more prevalent.

4. Other modifications of the lab set up could also have adjusted the prevalence of the fringes. For example, the baseline of the apertures on the mask where separated to the same distance as the diameter the columnizing lens. The baseline could not have been bigger than the lens but a larger baseline would have produced more fringes. A larger columnizing lens would have allowed for this.

5. Another step to take to get rid of the error in the recorded data is to try different methods of path error estimation. There are several methods besides using visibility to estimate path error. The changing phase of the fringe pattern can be used for path error estimation. It also should be possible to use a phase retrieval algorithm to estimate the path difference.

6. In order to use the piston model for the estimation of r_0 and L_0 a fringe correlation model, the correlation of two of more fringe patterns, should be developed using this work as a basis.

7. The correlation between piston and other Zernikes should be explored.

8. On sky data, or data recorded by means of a telescope observing a star or object in orbit, should be used in order to better compare this model to other variance models like that used by the differential image motion monitor or the general seeing monitor.

9. Future work could include building and testing a sensor for use in obtaining on sky, or real time, atmospheric parameters using this model. This sensor could even be patented.

10. In order to verify the simulated temporal correlation results data should be obtained that is orders more temporally correlated than that used in this research. There was a software limitation in this instance that kept the camera from recording images less than once per every second. A high speed camera can be used to rectify this limitation.

5.3 Significance and Impact

This research can directly impact the ability to simulate fringe and image jitter, which can help design better optical systems. It can also lead to less error in path delay systems that match the phases of interferometer paths which better resolutions of interferometers. Lastly, it can produce a new method of atmospheric seeing by using both image jitter and fringe jitter, or just fringe jitter, which can ultimately lead to better optical sensor technology and image resolution.

This research is a small step forward in solving a capability gap for the military and public space situational awareness communities. Ground based telescopes are far cheaper and sustainable than space based telescopes. In order for space battle management and planetary defense to thrive they need a mix of ground and space based radar assets along side efficient, high resolution ground based telescopes. This research can help close a capability gap in our space battle management and planetary defense systems.

Appendix A. Math Appendix

1.1 Covariance From Spatial to Wiener Spectrum

1.1.1 Transformation of Zernike Coefficient Variance to Wiener Spectrum from Spatial Domain

$$\left\langle a_j^* a_{j'} \right\rangle = \int\int\int\int A^*(u,v) Z_j^*(u,v) A(u',v') Z_{j'}(u',v') \Gamma_\theta(Ru'-Ru, Rv'-Rv) du dv du' dv' \tag{60}$$

Using the Wiener-Khinchin theorem on the phase covariance function we get:

$$= \int\int\int\int A^*(u,v) Z_j^*(u,v) A(u',v') Z_{j'}(u',v') ... \int\int R^{-2} \Phi_\theta(f_u/R, f_v/R) e^{i2\pi(f_u(u'-u)+f_v(v'-v))} df_u df_v du dv du' dv'$$

Defining the product of the aperture and Zernike polynomial as $A(u,v)Z_j(u,v) = P_j(u,v)$ allows us the write the equation as:

$$= \int\int\int\int P_j^*(u,v) P_{j'}(u',v') \int\int R^{-2} \Phi_\theta(f_u/R, f_v/R) e^{i2\pi(f_u(u'-u)+f_v(v'-v))} df_u df_v du dv du' dv'$$

Rearranging the equation gives:

$$= \int\int R^{-2} \Phi_\theta(f_u/R, f_v/R) \left[\int\int P_j^*(u,v) e^{-i2\pi(f_u u + f_v v)} du dv \right] ... \left[\int\int P_{j'}(u',v') e^{i2\pi(f_u u' + f_v v')} du' dv' \right] df_u df_v$$

$$= \int\int R^{-2} \Phi_\theta(f_u/R, f_v/R) Q_j^*(f_u, f_v) Q_{j'}(f_u, f_v) df_u df_v$$

$$= R^{-2} \int\int Q_j^*(f_u, f_v) Q_{j'}(f_u, f_v) \Phi_\theta(f_u/R, f_v/R) df_u df_v$$

1.1.2 Transformation of Zernike Coefficient Spatial Autocovariance to Wiener Spectrum from Spatial Domain

Remembering that spatial lengths were normalized by the radius of the apertures, any spatial shift would also need to normalized by the radius R. This leads to modifying equation 60 by the spatial shift B_x in the x-axis and by B_y in the y-axis for one coefficient.

$$\left\langle a_j^* a_{j'} \right\rangle = \int\int\int\int A^*(u,v) Z_j^*(u,v) A(u',v') Z_{j'}(u,v')... \\ \Gamma_\theta(Ru' - Ru + B_x, Rv' - Rv + B_y) du dv du' dv'$$

Using the Wiener-Khinchin theorem on the phase covariance function we get:

$$\left\langle a_j^* a_{j'} \right\rangle = \int\int\int\int A^*(u,v) Z_j^*(u,v) A(u',v') Z_{j'}(u',v')... \\ \int\int R^{-2} \Phi_\theta(f_u/R, f_v/R) e^{i2\pi(f_u(u'-u+B_x/R)+f_v(v'-v+B_y/R))} df_u df_v du dv du' dv'$$

Defining the product of the aperture and Zernike polynomial as $A(u,v)Z_j(u,v) = P_j(u,v)$ allows us the write the equation as:

$$= \int\int\int\int P_j^*(u,v) P_{j'}(u',v') \int\int R^{-2} \Phi_\theta(f_u/R, f_v/R)... \\ e^{i2\pi(f_u(u'-u+B_x/R)+f_v(v'-v+B_y/R))} df_u df_v du dv du' dv'$$

Rearranging the equation gives:

$$= \int\int R^{-2}\Phi_\theta(f_u/R, f_v/R)e^{i2\pi(f_uB_x/R+f_vB_y/R)}\left[\int\int P_j^*(u,v)e^{-i2\pi(f_uu+f_vv)}dudv\right]... \\ \left[\int\int P_{j'}(u',v')e^{i2\pi(f_uu'+f_vv')}du'dv'\right]df_udf_v$$

$$= \int\int R^{-2}\Phi_\theta(f_u/R, f_v/R)e^{i2\pi(f_uB_x/R+f_vB_y/R)}Q_j^*(f_u,f_v)Q_{j'}(f_u,f_v)df_udf_v$$

$$= R^{-2}\int\int Q_j^*(f_u,f_v)Q_{j'}(f_u,f_v)\Phi_\theta(f_u/R, f_v/R)e^{i2\pi(f_uB_x+f_vB_y)/R}df_udf_v$$

1.2 Multivariate Normal Conditional Mean and Covariance

According to the text "Multivariate Statistics: A Vector Space Approach" [25], page 116, for any multivariate normal random vector a vector space approach can be used to find a conditional mean and variance of an element of that random vector given the rest of the vector. The multivariate vector is partitioned into the element to be conditioned and the element that is being given as seen below:

$$\vec{x} = \begin{bmatrix} \vec{x}_1 \\ \vec{x}_2 \end{bmatrix}$$

These sub-vectors will have sizes of:

$$\begin{bmatrix} q \text{ x } 1 \\ (N-q) \text{ x } 1 \end{bmatrix}$$

These sub-vectors will have mean vectors of the same size:

$$\vec{\mu} = \begin{bmatrix} \vec{\mu}_1 \\ \vec{\mu}_2 \end{bmatrix}$$

Where N is the length of $\vec{x}$ and q is the length of $\vec{x}_1$. The covariance of the multivariate normal random vector is also partitioned:

$$\bar{\Sigma} = \begin{bmatrix} \bar{\Sigma}_{11} & \bar{\Sigma}_{12} \\ \bar{\Sigma}_{21} & \bar{\Sigma}_{22} \end{bmatrix}$$

This partitioned covariance will have sizes:

$$\begin{bmatrix} q \text{ x } q & q \text{ x } (N-q) \\ (N-q) \text{ x } q & (N-q) \text{ x } (N-q) \end{bmatrix}$$

The conditional mean is defined as:

$$E[\vec{x}_1|\vec{a}] = \hat{\mu} = \vec{\mu}_1 + \bar{\Sigma}_{12}\bar{\Sigma}_{22}^{-1}(\vec{a} - \vec{\mu}_2)$$

Where $\vec{a}$ is the realization of $\vec{x}_2$. The conditional variance is defined as:

$$Var[\vec{x}_1|\vec{a}] = \hat{\Sigma} = \bar{\Sigma}_{11} - \bar{\Sigma}_{12}\bar{\Sigma}_{22}^{-1}\bar{\Sigma}_{21}$$

Bibliography

1. The Very Large Telescope Interferometer, 2015.

2. MARKUS, COMERÓN, GLINDEMANN, HUMMEL, MOREL, PERCHERON, PETR-GOTZENS, and SCHÖLLER. OBSERVING WITH THE ESO VLT INTERFEROMETER. *The Messenger*, March(119), 2005.

3. NASA JWST FAQs.

4. Technical FAQ on a variety of mission issues, aspects and capabilities. (For the science/technical community.).

5. Magdalena Ridge Observatory Interferometer, 2014.

6. Robert J Noll. Zernike polynomials and atmospheric turbulence TL - 66. *Journal of the Optical Society of America*, 66 VN - r(3):207, 1976.

7. A. N. Kolmogorov. LOCAL STRUCTURE OF TURBULENCE IN AN INCOMPRESSIBLE VISCOUS FLUID AT VERY HIGH REYNOLDS NUMBERS. *Soviet Physics Uspekhi*, 10(6):734–746, 1968.

8. J W Goodman. *Statistical Optics*. Wiley, second edi edition, 1985.

9. Isaac B. Putnam and Stephen C. Cain. Modeling a Temporally Evolving Atmosphere with Zernike Polynomials. *AMOS Technical Conference*, 2012.

10. Jean-Marc Conan, Gérard Rousset, and Pierre-Yves Madec. Wave-front temporal spectra in high-resolution imaging through turbulence. *Journal of the Optical Society of America A*, 12(7):1559, 1995.

11. D. M. Winker. Effect of a finite outer scale on the Zernike decomposition of atmospheric optical turbulence. *Journal of the Optical Society of America A*, 8(10):1568, 1991.

12. V. V. Voitsekhovich. Outer scale of turbulence: comparison of different models. *Journal of the Optical Society of America A*, 12(6):1346, 1995.

13. R. Conan, J. Borgnino, A. Ziad, and F. Martin. Analytical solution for the covariance and for the decorrelation time of the angle of arrival of a wave front corrugated by atmospheric turbulence. *Journal of the Optical Society of America A*, 17(10):1807, 2000.

14. Aziz Ziad, Rodolphe Conan, Andrei Tokovinin, and Julien Borgnino. Seeing Monitor. *Applied Optics*, 39(30), 2000.

15. Naruhisa Takato and Ichirou Yamaguchi. Spatial correlation of Zernike phase-expansion coefficients for atmospheric turbulence with finite outer scale. *Journal of the Optical Society of America A*, 12(5):958, 1995.

16. Paulo P Andrade, Paulo J V Garcia, Carlos M Correia, Johann Kolb, and Maria Inês Carvalho. Estimation of atmospheric turbulence parameters from Shack–Hartmann wavefront sensor measurements. *Monthly Notices of the Royal Astronomical Society*, 483(1):1192–1201, 2018.

17. S. Esposito, A. Riccardi, and B. Femenía. Differential piston angular anisoplanatism for astronomical optical interferometers. *Astronomy and Astrophysics*, 353(3):29–32, 2000.

18. Gianluca Lombardi, Julio Navarrete, and Marc Sarazin. Review on atmospheric turbulence monitoring. *Adaptive Optics Systems IV*, 9148(July 2014):91481W, 2014.

19. Ioannis Nestoras. *The Theory Behind Seeing-GR and DIMM*. PhD thesis, Aristotle University of Thessaloniki, 2009.

20. A. Tokovinin. From Differential Image Motion to Seeing. *Publications of the Astronomical Society of the Pacific*, 114(800):1156–1166, 2002.

21. A. A. Michelson. ON THE APPLICATION OF INTERFERENCE METHODS TO ASTRONOMICAL MEASUREMENTS. *The Astrophysical Journal*, LI(5), 1920.

22. Peter R Lawson, editor. *Principles of long baseline stellar interferometry : course notes from the 1999 Michelson Summer School, August 15-19, 1999*. JPL Publication, 2000.

23. Stephen C. Cain and Majeed M. Hayat. Exploiting the Temporal Statistics of Atmospheric Tilt for Improved Short Exposure Imaging, 2001.

24. Richard D. Richmond and Stephen C. Cain. Direct-Detection LADAR Systems. In *Direct-Detection LADAR Systems*, chapter 3, pages 69–83. SPIE, 2010.

25. Morris Eaton. *Multivariate Statistics: a Vector Space Approach*. John Wiley and Sons, 1983.

REPORT DOCUMENTATION PAGE

Form Approved
OMB No. 0704–0188

1. REPORT DATE *(DD–MM–YYYY)*	2. REPORT TYPE	3. DATES COVERED *(From — To)*
27–03–2020	Master's Thesis	September 2018 — March 2020

4. TITLE AND SUBTITLE

Zernike Piston Statistics
in Turbulent Multi-Aperture Optical Systems

5a. CONTRACT NUMBER

5b. GRANT NUMBER

5c. PROGRAM ELEMENT NUMBER

6. AUTHOR(S)

Garretson, Joshua J., Capt, USAF

5d. PROJECT NUMBER

5e. TASK NUMBER

5f. WORK UNIT NUMBER

7. PERFORMING ORGANIZATION NAME(S) AND ADDRESS(ES)

Air Force Institute of Technology
Graduate School of Engineering and Management (AFIT/EN)
2950 Hobson Way
Wright-Patterson AFB OH 45433-7765

8. PERFORMING ORGANIZATION REPORT NUMBER

AFIT-ENG-MS-20-M-023

9. SPONSORING / MONITORING AGENCY NAME(S) AND ADDRESS(ES)

Captain Joseph Tompkins
EO Target Detection & Surveillance Branch
2241 Avionics Circle
Sensors Directorate, AFRL
WPAFB, OH 45433-7765

10. SPONSOR/MONITOR'S ACRONYM(S)

AFRL/RYMT

11. SPONSOR/MONITOR'S REPORT NUMBER(S)

12. DISTRIBUTION / AVAILABILITY STATEMENT

DISTRIBUTION STATEMENT A:
APPROVED FOR PUBLIC RELEASE; DISTRIBUTION UNLIMITED.

13. SUPPLEMENTARY NOTES

14. ABSTRACT

There is currently a lack of research into how the atmosphere effects Zernike piston. This Zernike piston is a coefficient related to the average phase delay of a wave. Usually Zernike piston can be ignored over a single aperture because it is merely a delay added to the entire wavefront. For multi-aperture interferometers though piston cannot be ignored. The statistics of Zernike piston could supplement and improve atmospheric monitoring, adaptive optics, stellar interferometers, and fringe tracking. This research will focus on developing a statistical model for Zernike piston introduced by atmospheric turbulence.

15. SUBJECT TERMS

Zernike Piston Statistics, Piston Differential, Interferometry, Fringe Tracking, Atmospheric Seeing, Outer Scale Measurement

16. SECURITY CLASSIFICATION OF:			17. LIMITATION OF ABSTRACT	18. NUMBER OF PAGES	19a. NAME OF RESPONSIBLE PERSON
a. REPORT	b. ABSTRACT	c. THIS PAGE			Dr. Stephen C. Cain, AFIT/ENG
U	U	U	UU	XXX	19b. TELEPHONE NUMBER *(include area code)* (937) 255-3636, ext 4716; Stephen.Cain@afit.edu